Energy 355 (2026) 141090

Contents lists available at ScienceDirect

Energy

journal homepage: www.elsevier.com/locate/energy

Distributionally robust location-inventory planning of commercial electric vehicle battery swapping stations with joint chance constraints

Xu Xin [a,1], Tao Zhang [b,c,*], King-Wah Pang [a], Jun Zhao [d], Shuaian Wang [a]

[a] Department of Logistics and Maritime Studies, Faculty of Business, The Hong Kong Polytechnic University, Hung Hom, Hong Kong Special Administrative Region, PR China

[b] School of Economics and Management, Tongji University, Shanghai, 200092, PR China

[c] Department of Industrial and Systems Engineering, Faculty of Engineering, The Hong Kong Polytechnic University, Hung Hom, Hong Kong Special Administrative Region, PR China

[d] Laboratory of Efficient Utilization of Low and Medium Grade Energy, School of Mechanical Engineering, Tianjin University, Tianjin, 300350, PR China

ARTICLE INFO

Keywords:
Commercial electric vehicle
Battery swapping station location
Demand uncertainty
Distributionally robust optimization
Outer approximation algorithm

ABSTRACT

The electrification of commercial electric vehicle fleets is constrained by long charging times and insufficient infrastructure. Battery swapping stations (BSSs) offer a promising alternative, yet their strategic deployment is complicated by uncertain spatial demand and stringent service requirements. In this paper, the commercial electric vehicle BSS location-inventory problem is investigated through a two-stage distributionally robust optimization (DRO) framework with a joint chance constraint. Using moment-based ambiguity sets, we derive a tractable second-order cone programming reformulation via a conditional value-at-risk approximation and solve it with a tailored outer approximation algorithm. Numerical experiments on standard transportation networks, together with benchmark tests against commercial solver DICOPT, confirm the computational tractability and scalability of the proposed approach. Sensitivity analyses further reveal how ambiguity, transportation cost, inventory capacity, construction cost, and reliability requirements shape battery inventory deployment and network configuration. Finally, out-of-sample comparisons with stochastic programming and robust optimization benchmarks show that the DRO framework provides a more balanced trade-off between cost and reliability, maintaining strong network-wide service performance under multiple demand distributions.

1. Introduction

Driven by the critical imperative to decarbonize global transportation and mitigate greenhouse gas (GHG) emissions [1,2], the electrification of the transport sector is accelerating rapidly [3,4]. Electric vehicles (EVs) offer immediate environmental benefits [5,6], prompting widespread government subsidies [7] and ambitious market share targets [8], including mandates to phase out gasoline vehicles [9]. During this transition, commercial vehicles, such as taxis and ride-sourcing services (e.g., Uber[2] and DiDi Chuxing), play a pivotal role because of their massive daily transit volumes. The proven economic viability of commercial electric vehicles (CEVs) [9], supported by EV technology advancements [10] and green fiscal incentives [11], has made CEVs serve as a pragmatic pathway for sustainable urban mobility, with megacities such as Shenzhen, China already achieving full-fleet electrification [12].

However, widespread CEV deployment faces formidable bottlenecks: prohibitively long charging times [13] and scarce charging infrastructure [14], which contradict the rigorous operational efficiency prioritized by CEV drivers [1]. Frequent fast charging [15] accelerates battery degradation [13] and exacerbates power grid overloads [16]. Furthermore, the current charging facility supply often fails to meet surging urban demand [17], while suboptimal locations lead to underutilization and poor return on investment [3]. To circumvent these impediments, battery swapping stations (BSSs) [18] have emerged as a robust solution. BSSs facilitate rapid exchanges of depleted batteries for fully charged units (often under 90 s) [10,19,20], reduce battery degradation via unified slow charging [21], and require significantly less land area than

* Corresponding author. School of Economics and Management, Tongji University, Shanghai, 200092, PR China.
E-mail addresses: xu-david.xin@connect.polyu.hk, x.xin@polyu.edu.hk (X. Xin), taozhang@tongji.edu.cn, tao-zt.zhang@connect.polyu.hk (T. Zhang), anthony.pang@polyu.edu.hk (K.-W. Pang), zhaojun@tju.edu.cn (J. Zhao), hans.wang@polyu.edu.hk (S. Wang).
[1] http://xinxu.space/xinxu-en
[2] https://investor.uber.com/news-events/news/press-release-details/2025/Uber-Announces-Results-for-Fourth-Quarter-and-Full-Year-2024/default.aspx.

https://doi.org/10.1016/j.energy.2026.141090
Received 16 February 2026; Received in revised form 16 April 2026; Accepted 17 April 2026
Available online 21 April 2026
0360-5442/

traditional charging stations do [22]. Driven by these advantages, BSS deployment is accelerating rapidly worldwide (e.g., NIO and Aulton[3] networks).

Despite this momentum, developing a scalable BSS infrastructure presents a complex decision-making challenge: optimizing the BSS locations and battery inventory levels under demand uncertainty. CEV swapping demand is highly unpredictable due to commuting dynamics, seasonality [23], and heterogeneity in the behavior of CEV drivers of battery performance [3]. Misalignment between BSS locations and inventories can induce substantial operational friction and fiscal loss [24]. We formalize this specific challenge as a **C**EV **B**SSs **L**ocation and **I**nventory **P**roblem considering battery swapping demand uncertainty (CBLIP), assuming that enterprise decision makers plan a dedicated BSS system rather than relying on a mixed public-refueling environment.

To address decision-making under uncertainty, researchers have typically relied on stochastic programming [25,26] and robust optimization [27,28]. However, a critical research gap remains regarding their application to emerging systems such as the CBLIP [29]. Stochastic programming relies heavily on the assumption that the exact probability distribution function (PDF) of the uncertain parameter is known. In practice, obtaining accurate PDFs is often impossible for CEV transportation networks where historical data are sparse, leading to poor out-of-sample performance. Conversely, robust optimization ignores probability entirely, making decisions based on extreme worst-case scenarios governed by uncertainty sets. This method produces excessively conservative solutions that are resource heavy and economically inefficient. Thus, previous research lacks a methodological framework capable of handling ambiguous spatial demand without falling into either over-optimism or extreme conservatism. To bridge this gap, distributionally robust optimization (DRO) provides a viable pathway [30]. By constructing an ambiguity set from available statistical data (e.g., moments), DRO minimizes costs under the worst-case distribution within this set, delivering solutions that are reliable and cost-effective without requiring exact PDFs. Unlike existing studies that utilize the Wasserstein metric or Kullback–Leibler (KL) divergence to construct ambiguity sets, this paper adopts a moment-based framework. While Wasserstein and KL-based DRO are data driven in nature, they often lead to high-dimensional optimization problems where the number of constraints scales with the sample size. In the context of our CBLIP, which involves discrete investment decisions and joint reliability requirements, the moment-based approach provides a more parsimonious and computationally tractable representation, ensuring that the resulting model remains independent of the empirical sample scale.

Motivated by these theoretical advancements and the identified research gaps, the primary objective of our paper is to provide decision makers with a data-driven tool that balances investment efficiency with operational robustness for CBLIP. To achieve this objective, the novelty of our paper is reflected in three aspects. First, we develop a novel two-stage DRO model with a joint chance constraint. Unlike previous studies, our framework jointly determines strategic station locations and pre-positioned battery inventories (first stage) and operational demand allocation (second stage) while explicitly enforcing network-wide service reliability. Second, to overcome the intractability of the original DRO formulation, we derive an exact analytical reformulation. By exploiting the conditional value at risk (CVaR), we convert the complex joint chance constraint into a parametric second-order cone programming (SOCP) model. Third, we develop a tailored outer approximation algorithm (OAA) that exploits the convex conic structure of our reformulated model, ensuring computational tractability and exact solutions for large-scale CEV network planning.

The remainder of this paper is organized as follows. Section 2 reviews the related literature from the perspectives of modeling ideas and solution methodologies. Section 3 describes CBLIP and formulates the model. Section 4 presents the reformulation procedure, and Section 5 develops the solution algorithm. Numerical experiments are reported in Section 6. Section 7 extends the analysis to mobile battery swapping facilities. Section 8 concludes the paper and discusses future research directions.

2. Literature review

The CBLIP is a specialized variant of the facility location problem (FLP). In recent years, although FLP research has covered diverse domains in transportation and logistics, such as medical centers [31], waste treatment plants [32], warehouses in emergency management [33], and drone base stations [34], research dedicated to BSS locations remains relatively rare [3]. A preponderance of the extant research still focuses on EV charging stations. Interested readers may also consult review papers [35] and [36] on the charging station location problem. Given the structural parallels between the two research subjects, this section reviews the literature on the EV charging station location problem and the BSS location problem and their solution methodologies to identify research gaps. Furthermore, to provide a comprehensive overview, detailed comparisons of representative studies from both the research-content and methodological perspectives are summarized in Appendix M of the supplementary material.

2.1. EV charging station/BSS location model

Drawing upon the taxonomy established by Guo et al. [3], the EV charging station/BSS location problem can be broadly bifurcated into two streams based on whether the parameters are known: *deterministic models* and *nondeterministic models*. The former presumes that all the parameters in the model are fixed and known; the latter, on the other hand, incorporates parametric uncertainty. In recent years, scholars have constructed a series of different types of deterministic models. For example, leveraging theories such as the analytic hierarchy process and the fuzzy decision-making trial and evaluation laboratory, Mallahi et al. [37] constructed an evaluation model to assess the ideal BSS location in four districts of Beijing, China. Similarly, Türk et al. [38] applied a multi-criteria decision-making method to select the locations of charging stations. In contrast, Li et al. [39] used Cournot's competitive game theory to optimize a competitive resource allocation strategy for charging pile planning. However, this method can describe only trends and cannot obtain quantitative solutions. With the advancement of mathematical optimization theory, scholars still opt to construct mathematical optimization models to seek quantitative solutions to the FLP associated with EV charging stations or BSSs [40]. For example, Hof et al. [41] integrated BSS location and EV routing into a joint optimization problem and aimed to minimize the sum of BSS construction costs and routing costs. Lai and Li [14] considered the locations of both charging stations and BSSs to meet the demands of EV ride-hailing fleets.

Nevertheless, the aforementioned literature does not consider uncertainty factors. With the development of uncertain programming theory, developing nondeterministic models (including stochastic programming and robust optimization) has become the mainstream modeling approach for dealing with uncertainty. When using stochastic optimization theory, scholars usually need to assume that the decision maker knows the PDFs of uncertain parameters so that they can try to transform the uncertain parameters contained in the model. For example, Lin et al. [42] investigated the location problem of scooter BSSs. The authors considered both the average driving distance of the BSS and the BSS construction cost as dual objectives and designed a Nondominated Sorting Genetic Algorithm-II (NSGA-II) to solve the model. Zhou et al. [43] constructed a two-stage stochastic programming model to address the electric bus charging facility location problem while considering the uncertainties of the EV driving time and battery degradation. Similarly, Esmaeilnejad et al. [44] proposed a similar model structure to capture the uncertainties associated with the demand

[3] https://www.aulton.net.cn/en/show-28-126.html.

and performance of a battery (caused by weather conditions). Conversely, as an effective method for dealing with uncertainty in problems, robust optimization does not require the assumption that the distribution functions of uncertain parameters are known [45]. Studies employing this modeling approach include Liu and Song [46], who addressed a wireless charging infrastructure location problem using electric buses as the research subject. To describe the uncertainty, the authors assumed that the ranges of energy consumption and travel time lie within two uncertain sets. Alwesabi et al. [47] modeled a similar problem, with the difference being that they focused on the uncertainty of energy demand and included charging time as a decision variable in the model. Guo et al. [3] constructed a robust optimization model to achieve joint optimization of BSS location and battery inventory management in each BSS. The authors assumed that the battery swapping demand faced by each BSS is an uncertain parameter. On the basis of the Benders decomposition concept, the authors specifically addressed algorithms for solving the model. Li et al. [48] addressed a similar problem, but they focused on charging stations rather than BSSs. Since the charging time of EVs cannot be ignored, a series of constraints are introduced into the model to characterize the congestion at charging stations.

However, none of the above studies considered the endogenous interaction between travelers and networks. In fact, as some candidate nodes in the transportation network deploy charging stations or BSSs, travelers' route choice behavior in the transportation network shifts because they have more options. This has spurred the use of network equilibrium models to determine the locations for charging stations or BSSs [35]. For example, He et al. [49] developed a nonlinear programming model to formulate a tour-based network equilibrium state. Using this model, the authors implemented an EV charging station deployment that takes energy consumption uncertainty into account. Based on [49], He et al. [50] further constructed a bi-level programming model considering the driving range of EVs. To solve this model, the authors reconstructed the original model into a single-level model and used linearization techniques to ultimately convert it into a linear model, thereby developing a heuristic algorithm to solve this model.

Recently, the literature has increasingly examined risk-aware BSS planning within broader energy ecosystems, highlighting the role of BSSs as flexible storage in renewable-integrated microgrids and multi-energy hubs. Scenario-based stochastic programming and financial risk measures such as CVaR have been used in long-term expansion planning [51,52], day-ahead energy management [51,53], and the operation of hybrid all-in-one vehicle stations [54]. However, these studies address mainly operational risk mitigation and grid integration under known probability distributions, whereas our paper considers the strategic location-inventory problem under demand uncertainty within a distributionally robust framework.

Overall, the literature shows a clear shift from deterministic formulations to uncertainty-aware models for charging station and BSS planning. Some studies further incorporate network equilibrium to capture travelers' route-choice responses. With respect to modeling uncertainty, stochastic programming and robust optimization remain dominant, whereas DRO-based research is still limited and has focused mainly on BSS inventory management [29], charging scheduling [55] and charging station locations [40,56]. The study closest to ours is Guo et al. [57], which introduced a two-stage DRO model for BSS location planning. Their work demonstrated mainly the feasibility of combining DRO and joint chance constraints in BSS planning. Our paper goes further by refining the demand representation for cost evaluation and, more importantly, by developing a tractable reformulation and scalable exact solution framework for larger instances. Moreover, existing DRO studies employ different ambiguity sets, including moment-based, KL divergence-based, moment-KL hybrid, and Wasserstein-metric sets. These classes offer different trade-offs between statistical richness and computational tractability. For our CBLIP with discrete location decisions and a network-wide joint chance constraint, the moment-based set is adopted not because it is universally superior but because it is structurally most compatible with the present model. KL-type and hybrid sets typically require a reliable nominal distribution and lead to more involved entropy-type dual reformulations, whereas Wasserstein-based sets are often sample-size dependent and become much more difficult to reformulate tractably under joint chance constraints. In contrast, the moment-based set relies only on first- and second-order information, which is more realistic in data-scarce strategic planning, and it directly supports conic reformulations. Therefore, the advantage of the adopted ambiguity set in this paper lies in its ability to balance data pragmatism, reliability modeling, and exact tractable solution methodology within a unified framework.

Despite the growing use of DRO in energy and transportation, the literature remains fragmented. First, many risk-aware BSS studies focus on operational problems under known distributions rather than strategic planning under distributional ambiguity. Second, most charging-station/BSS planning studies emphasize either facility location or uncertainty treatment but not the joint design of location, battery inventory, or network-wide service reliability. Third, despite the limited BSS literature on the use of DRO, methodological attention rarely extends beyond model construction to exact reformulation and scalable solution design. In this context, we study a strategic CEV BSS location-inventory problem under ambiguous spatial demand, impose a joint chance constraint to ensure system-wide reliability, derive a tractable SOCP reformulation via the CVaR approximation, and develop a tailored OAA for large-scale instances. Thus, the contribution of this paper lies not in using DRO alone but in the integration of strategic network design, distributional ambiguity, reliability control, and exact tractable solution methodology within one unified framework.

2.2. Solution methodologies

Current solution methods can be broadly divided into (meta)heuristics and exact methods. Metaheuristic methods seek near-optimal solutions and are often used for large-scale problems or models with non-differentiable, discontinuous, or highly nonlinear structures [58]. Typical examples include biologically or physically inspired methods such as genetic algorithms and simulated annealing [59]. However, for uncertainty-intensive models, heuristics have notable limitations: they may suffer from the curse of dimensionality, struggle to identify robustly feasible regions [60], and provide limited control over worst-case uncertainty.

With the development of uncertain optimization theory in recent years, recent studies have shifted toward exact methods. Methods such as Benders decomposition, column-and-constraint generation (CCG), and Lagrangian relaxation are being increasingly adopted to ensure that solutions meet strict optimality bounds. For example, Zhao et al. [61] demonstrated that Benders-based frameworks can effectively decouple strategic BSS locations from operational charging subproblems, transforming complex robust formulations into tractable mixed-integer linear programming (MILP) models. On the basis of this solution method, Guo et al. [3] conducted similar research. Scholars have also proposed a series of techniques to accelerate the model-solving process, such as strengthening the model formulations, introducing valid inequalities, and reducing the values of big-M coefficients [62–64].

Despite their theoretical rigor, exact methods for DRO in BSS locations remain underexplored because of their complexity in implementation. The effectiveness of these methods hinges on the reformulation of the model based on the ambiguity set and the design of efficient acceleration strategies that can handle the nonconvex feasible regions of DRO models with chance constraints. To bridge this critical gap, we construct a two-stage DRO model with a joint chance constraint and develop a tailored exact solution framework based on the outer approximation to solve the reformulated model efficiently.

3. Problem description and model formulation

To help readers grasp the overall structure of the paper, Fig. 1 presents the research framework. It summarizes the logical progression from problem description and model formulation to reformulation and algorithm design. In this section, Section 3.1 provides the problem description of CBLIP and the assumptions and notations used. Section 3.2 describes the construction of the mathematical model for solving CBLIP.

3.1. Problem description

In this paper, we consider a transportation system that supports CEV battery swapping. This system contains two types of nodes: (1) battery swapping demand generation nodes and (2) candidate location nodes for BSS construction. The sets formed by these two types of nodes are denoted as $\mathscr{O} = \{1, 2, 3, \cdots, O\}$ and $\mathscr{D} = \{1, 2, 3, \cdots, D\}$, respectively. Each element in set $\mathscr{O}$ represents a node where battery swapping demand is generated. The aforementioned demand is further divided into the (daily) total battery swapping demand and the (daily) necessary battery swapping demand generated by node $i \in \mathscr{O}$. These two types of demand are characterized by two random variables, i.e., ξ_i and ζ_i, respectively. The former (ξ_i) refers to the total number of CEVs that require swap batteries (in 24 h), and the latter (ζ_i) refers to the number of CEVs whose batteries must be swapped to maintain operation. The difference lies in the fact that the former category includes some drivers who have sufficient CEV battery charge but still wish to swap batteries (e.g., owing to personal preference).

To fulfill the battery swapping demands in this transportation system, the decision maker (e.g., the strategic management department of a certain company) needs to select several nodes from $\mathscr{D}$ to construct BSSs. In the first stage of the model, we define a binary decision variable x_j to indicate whether candidate location $j \in \mathscr{D}$ is selected to construct a BSS. When x_j equals 1, the decision maker chooses to construct a BSS at node $j \in \mathscr{D}$; otherwise, it is 0. The (daily) construction cost of constructing a BSS at node $j \in \mathscr{D}$ is c_j. Moreover, to support battery swapping for the CEVs, each BSS $j \in \mathscr{D}$ needs to be pre-positioned with a certain number of batteries, denoted as y_j. Owing to the limited space of the BSS, we assume that if a BSS is constructed at node $j \in \mathscr{D}$, it can pre-position a maximum of $\bar{y}_j$ batteries. The (daily) battery purchase and holding cost (mainly maintenance cost) at node $j \in \mathscr{D}$ is h_j.

We assume that the battery swapping demand generated by each node $i \in \mathscr{O}$ (i.e., ξ_i and ζ_i) can be satisfied by any BSS in the system. However, external public swapping (or charging) stations are not explicitly incorporated as service facilities. The difference lies in the fact that CEVs incur different transportation costs when traveling to different BSSs, and the battery degradation costs vary across different BSSs. We set the transportation distance from node $i \in \mathscr{O}$ to the candidate location $j \in \mathscr{D}$ to be d_{ij}. The unit transportation cost for a CEV is denoted as β. If a CEV with battery swapping demand at node $i \in \mathscr{O}$ chooses to travel to location $j \in \mathscr{D}$ to satisfy its demand, then the resulting transportation cost is βd_{ij}. The unit battery (daily) degradation cost at node $j \in \mathscr{D}$ is set to γ_j. To control the aforementioned transportation costs, the decision maker can determine which BSS is to be utilized to satisfy the demand generated at node $i \in \mathscr{O}$. In the second-stage model, we introduce a continuous decision variable $z_{ij} \in [0, 1]$ to represent the percentage of demand generated by node $i \in \mathscr{O}$ served by the BSS constructed at node $j \in \mathscr{D}$. For example, $z_{12} = 0.25$ indicates that 25% of the demand generated by Node 1 is satisfied by the BSS constructed at Node 2.

Based on the above background, the optimization objective of CBLIP is to minimize total costs (including BSS construction costs, battery procurement and holding costs, and CEV transportation costs). The decision maker needs to find the optimal BSS locations $\boldsymbol{x} = (x_j)$, inventory levels (i.e., pre-positioned battery quantity) of each BSS $\boldsymbol{y} = \left(y_j\right)$, and demand-fulfilling scheme (i.e., which demand generation nodes each BSS should serve and the corresponding demand fulfillment levels) $\boldsymbol{z} = (z_{ij})$ while ensuring that each BSS can simultaneously meet the predetermined service level, i.e., $1 - \alpha$. In other words, we require that the probability of the event that *all necessary battery swapping demand quantities allocated to all the BSSs are satisfied* is greater than or equal to $1 - \alpha$.

For modeling convenience, we introduce the following assumptions. (1) All the CEVs have the same battery model and configuration [3]. This

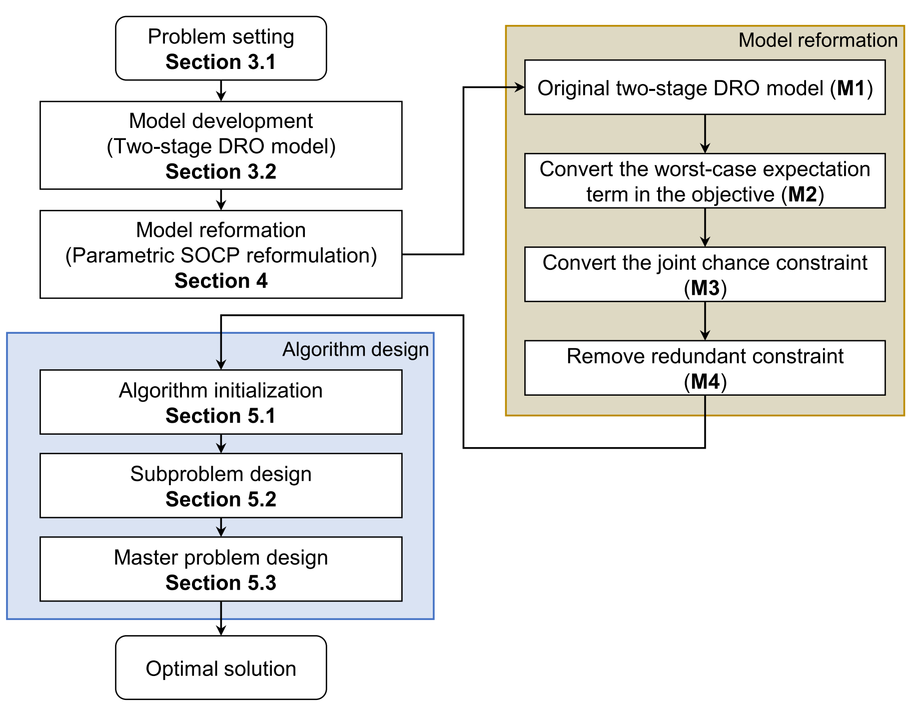

Fig. 1. Research framework.

assumption can be relaxed by introducing different types of CEVs and batteries. (2) The demand generated at each demand generation node can be satisfied by any BSS. This assumption can be relaxed by adding a constraint that defines the service area of each BSS. (3) Since the uncertainty of battery swapping demand is affected by both the user and the system level, we assume that the distribution function of demand is difficult to obtain. However, decision makers always have limited information available. (3) After the battery swap is completed by the BBS, the CEV can move freely in the transportation system. For the convenience of readers, the notations commonly used are listed in the table in Appendix J of the supplementary material.

3.2. Model development

In this section, a two-stage DRO model for solving our CBLIP is constructed, abbreviated as **M1**. The expression for the first stage of **M1** is as follows. This model is developed based on the robust optimization model proposed by Guo et al. [3] and Guo et al. [57].

3.2.1. First stage of M1

$$\min_{(\boldsymbol{x},\boldsymbol{y})}\left\{\sum_{j\in\mathscr{D}}\left(c_jx_j+h_jy_j\right)+\sup_{F\in\mathscr{F},G\in\mathscr{G}}\mathbb{E}_{F,G}[g(\boldsymbol{n},\boldsymbol{\xi},\boldsymbol{\zeta})]\right\} \tag{1}$$

$$s.t.\ y_j\le\overline{y}_jx_j\ \forall j\in\mathscr{D} \tag{2}$$

$$\boldsymbol{x}\in\{0,1\}^{|\mathscr{D}|} \tag{3}$$

$$\boldsymbol{y}\in\mathbb{Z}_+^{|\mathscr{D}|} \tag{4}$$

where $\boldsymbol{x}=(x_j)$; $\boldsymbol{y}=\left(y_j\right)$; $\boldsymbol{\xi}=(\xi_i)$; $\boldsymbol{\zeta}=(\zeta_i)$; $\mathbb{Z}_+$ represents the set of all non-negative integers; and $\boldsymbol{n}$ is a vector consisting of all the decision variables in the first-stage model, i.e., $\boldsymbol{n}=(\boldsymbol{x},\boldsymbol{y})$.

In the above equations, Equation (1) is the objective function of the model, which aims to minimize the expected total cost. Specifically, the first term $\sum_{j\in\mathscr{D}}\left(c_jx_j+h_jy_j\right)$ calculates the construction cost of the BSS and the purchase and holding costs of the battery. The second term is used to calculate the worst-case scenario for the expected *second-stage cost*, i.e., $g(\boldsymbol{n},\boldsymbol{\xi},\boldsymbol{\zeta})$. Here, F and G represent the distribution functions of $\boldsymbol{\xi}$ and $\boldsymbol{\zeta}$, respectively. We assume that they are unknown but are governed by two ambiguity sets, i.e., $\mathscr{F}$ and $\mathscr{G}$. In other words, $\sup_{F\in\mathscr{F},G\in\mathscr{G}}\mathbb{E}_{F,G}[g(\boldsymbol{n},\boldsymbol{\xi},\boldsymbol{\zeta})]$ denotes the expected cost under the worst-case distributions governed by sets $\mathscr{F}$ and $\mathscr{G}$. Constraint (2) requires that if node $j\in\mathscr{D}$ is selected to construct a BSS, then it can pre-position a maximum of $\overline{y}_j$ batteries. Constraints (3) and (4) give the domain of the decision variables involved in the first-stage model.

The second stage of **M1** is shown below.

Second stage of M1:

$$g(\boldsymbol{n},\boldsymbol{\xi},\boldsymbol{\zeta})=\min_{\boldsymbol{z}}\sum_{i\in\mathscr{O}}\beta\xi_i\sum_{j\in\mathscr{D}}d_{ij}z_{ij}+\sum_{i\in\mathscr{O}}\xi_i\sum_{j\in\mathscr{D}}\gamma_jz_{ij} \tag{5}$$

$$s.t.\ \sum_{j\in\mathscr{D}}z_{ij}=1\ \forall i\in\mathscr{O} \tag{6}$$

$$z_{ij}\le x_j\ \forall i\in\mathscr{O},j\in\mathscr{D} \tag{7}$$

$$\mathbb{P}_G\left(\sum_{i\in\mathscr{O}}\zeta_iz_{ij}\le y_j,\forall j\in\mathscr{D}\right)\ge1-\alpha\ \forall G\in\mathscr{G} \tag{8}$$

$$z_{ij}\le1\ \forall i\in\mathscr{O},j\in\mathscr{D} \tag{9}$$

$$\boldsymbol{z}\in\mathbb{R}_+^{|\mathscr{O}|\times|\mathscr{D}|} \tag{10}$$

where $\boldsymbol{z}=(z_{ij})$ and $\mathbb{R}_+$ denotes the set of all non-negative real numbers.

Objective function (5) is used to minimize the total transportation cost of the CEV in the system. Constraint (6) requires that the demand at each demand generation node be fully allocated to the BSSs in the system. Constraint (7) gives the relationship between variables z_{ij} and x_j. Constraint (8) is a joint chance constraint. It requires that the probability of the event in which *all necessary battery swapping demand quantities allocated to all the BSSs are satisfied* is greater than or equal to $1-\alpha$, where $1-\alpha$ is also known as the service level. Constraints (9) and (10) define the domain of the decision variable z_{ij}.

Although **M1** captures the strategic planning logic of CBLIP, it is not directly solvable in its original form. The computational difficulty arises from two sources: the worst-case expectation term in the first-stage objective and the non-convex joint chance constraint in the second stage. Therefore, the overall solution framework of this paper proceeds in two layers. We first reformulate **M1** into a tractable parametric SOCP through a sequence of analytical transformations. We then solve the reformulated model by a tailored OAA. Accordingly, Section 4 focuses on tractable reformulation, whereas Section 5 develops the exact solution framework built on the reformulated model.

4. Model reformation

Before presenting the mathematical details, we briefly outline the reformulation logic. The original **M1** is difficult to solve because the objective contains a worst-case expectation term over an ambiguity set, and the constraints include a joint chance constraint. We therefore proceed in three steps: First, we reformulate the worst-case expectation term in the objective to obtain **M2**; second, we reformulate the joint chance constraint to derive **M3**; and third, we remove a redundant constraint and obtain the final tractable model **M4**.

4.1. Objective function

Examining the structure of function (5), we find that a linear relationship exists between the objective function values $\beta\sum_{i\in\mathscr{O}}\xi_i\sum_{j\in\mathscr{D}}d_{ij}z_{ij}+\sum_{i\in\mathscr{O}}\xi_i\sum_{j\in\mathscr{D}}\gamma_jz_{ij}$ and $\boldsymbol{\xi}$ in the second-stage model. Moreover, if decision $\boldsymbol{n}=(\boldsymbol{x},\boldsymbol{y})$ is known, the optimal solution of the second-stage cost function is affected by only three parameters (i.e., β, γ_j and d_{ij}) and the realization of a random variable (ξ_i). From this perspective, the value of $\mathbb{E}_{F,G}[g(\boldsymbol{n},\boldsymbol{\xi},\boldsymbol{\zeta})]$ is controlled solely by the expected ξ_i. Thus, to address the uncertainty in Equation (5), we assume that the distribution function of $\boldsymbol{\xi}$ is F and construct an ambiguity set to govern $\mathscr{F}$, which is sufficient to consider $\mathscr{F}$ with an uncertain first moment. We let $\boldsymbol{\mu}>\boldsymbol{0}$ and $\boldsymbol{\Sigma}\succeq0$ be the estimated expectation and covariance matrix of $\boldsymbol{\xi}$ obtained by observing historical data. On the basis of the mean-covariance information, we set the expression for $\mathscr{F}$ as follows:

$$\mathscr{F}=\left\{F:(\mathbb{E}_F[\boldsymbol{\xi}]-\boldsymbol{\mu})^{\mathrm{T}}\boldsymbol{\Sigma}^{-1}(\mathbb{E}_F[\boldsymbol{\xi}]-\boldsymbol{\mu})\le\varepsilon_1^2\right\} \tag{11}$$

where the coefficient $\varepsilon_1>0$.

In Equation (11), choosing an appropriate coefficient $\varepsilon_1\in\mathbb{R}_{++}$ is crucial [65]. If the value is too large or too small, it is not conducive to obtaining an effective solution. Clearly, the above choice depends on an accurate estimate of the first moment. To achieve this goal, we draw on the technique proposed by Delage and Ye [66]. In Section 3 of [66], the authors develop an efficient method for estimating ε_1 on the basis of samples. In particular, we assume that the decision maker can obtain a set of M independent samples of random variable $\boldsymbol{\xi}=(\xi_i)$, i.e., set $\{\widehat{\boldsymbol{\xi}}_1,\widehat{\boldsymbol{\xi}}_2,\widehat{\boldsymbol{\xi}}_3,\cdots,\widehat{\boldsymbol{\xi}}_M\}$, and calculate the sample mean and covariance matrix. We also suppose that $\mathbb{E}[\boldsymbol{\xi}]=\boldsymbol{\mu}_0$ and that $\mathrm{Cov}[\boldsymbol{\xi}]=\boldsymbol{\Sigma}_0$. **Corollary 2** in [66] clarifies that for all $\delta>0$, if we have $\mathbb{P}\left\{(\boldsymbol{\xi}-\boldsymbol{\mu}_0)^{\mathrm{T}}\boldsymbol{\Sigma}_0^{-1}(\boldsymbol{\xi}-\boldsymbol{\mu}_0)\le\delta^2\right\}=1$, then inequality $(\boldsymbol{\mu}_0-\widehat{\boldsymbol{\mu}})^T\boldsymbol{\Sigma}_0^{-1}(\boldsymbol{\mu}_0-\widehat{\boldsymbol{\mu}})\le\tau(\delta)$ can be satisfied with a probability greater than $1-\delta$ over the choice of $\{\widehat{\xi}_1,\widehat{\xi}_2,\widehat{\xi}_3,\cdots,\widehat{\xi}_M\}$, where $\boldsymbol{\mu}_0 = 1/M\sum_{i=1}^{M}\hat{\boldsymbol{\xi}}_i$ and $\tau(\delta) = (R^2/M)\left[2+\sqrt{2\ln(1/\delta)}\right]^2$. **Corollary 4** in [66] also provides a technique for determining ε_1 when R and $\boldsymbol{\Sigma}_0$ are unknown. Using the above properties, we propose Proposition 1 to reconstruct model **M1**.

Proposition 1. ***M1*** *can be equivalently converted as follows*:

M2:

$$\min\sum_{j\in\mathscr{D}}\left(c_jx_j+h_jy_j\right)+\varepsilon_1\theta+\boldsymbol{\mu}^{\mathrm{T}}\boldsymbol{m} \tag{12}$$

s.t. (2), (3), (4), (6), (7), (8), (9), (10),

$$m_i=\sum_{j\in\mathscr{D}}\left(\beta d_{ij}+\gamma_j\right)z_{ij}\ \forall i\in\mathscr{O} \tag{13}$$

$$\left\|\boldsymbol{\Sigma}^{1/2}\boldsymbol{m}\right\|\le\theta \tag{14}$$

where $\boldsymbol{m}=(m_i)\in\mathbb{R}_+^{|\mathscr{O}|}$ and $\theta\in\mathbb{R}_+$ are newly introduced auxiliary variables.

Proof. Please refer to Appendix A of the supplementary material. (Q. E. D.)

By simplifying the second-stage cost into a linear form and applying the minimax inequality, the intractable supremum operation can be transformed. The inner maximization problem over the ellipsoidal set is then solved analytically, leading to second-order cone reformulation, as proven in Appendix A.

Remark 1. While ambiguity sets based on the Wasserstein metric have recently gained traction due to their strong asymptotic convergence properties, this paper deliberately adopts a moment-based ambiguity set for two reasons. First, historical data for large-scale BSS operations are often sparse or subject to corporate confidentiality, making the construction of sample-based sets (e.g., Wasserstein-based sets) prone to over-fitting or computational intractability. In contrast, macroscopic statistics such as the mean and covariance are more accessible and can be reliably estimated from initial pilot operations or driver surveys. Furthermore, the reliability of these estimates is explicitly addressed by the calibration of ε_1. As the sample size M decreases or the estimation uncertainty increases, the radius ε_1 automatically expands based on the Delage and Ye [66] framework, leading to a more robust and conservative decision to hedge against potential estimation errors.

4.2. Joint chance constraint

We assume that the decision maker can obtain the sample mean ($\boldsymbol{u}$) and covariance information ($\boldsymbol{\Gamma}$) of the necessary demand ($\boldsymbol{\zeta}$) by collecting historical data. We define the ellipsoid ambiguity set that governs function G as follows:

$$\mathscr{G}:=\left\{G:\begin{array}{c}(\boldsymbol{\zeta}-\boldsymbol{u})^{\mathrm{T}}\boldsymbol{\Gamma}^{-1}(\boldsymbol{\zeta}-\boldsymbol{u})\le\varepsilon_2^2\\ \mathbb{E}_G[\boldsymbol{\zeta}]=\boldsymbol{u}\\ \mathbb{E}_G\left[\boldsymbol{\zeta}^2\right]=\boldsymbol{u}^{\mathrm{T}}\boldsymbol{u}+\boldsymbol{\Gamma}\end{array}\right\}. \tag{15}$$

The ambiguity sets commonly adopted by scholars also include box ambiguity sets. However, some scholars note that using such an ambiguity set can easily lead to overly-conservative solutions [67]. This prompts us to use the ellipsoid ambiguity set, which has been thoroughly examined by Chen et al. [68].

Remark 2. While ambiguity sets based on the Wasserstein metric, KL divergence, and their hybrids have attracted increasing attention in DRO, this paper adopts a moment-based ambiguity set. From a practical perspective, strategic BSS planning often faces limited and fragmented historical data, especially for newly developed urban districts. In such settings, reliable estimation of the mean vector and covariance matrix is typically more realistic than specifying a trustworthy nominal distribution or constructing a high-fidelity empirical distribution from large samples. From a computational perspective, the present model combines binary location decisions with a network-wide joint chance constraint. Under this structure, KL-based and moment–KL hybrid sets generally lead to more complicated dual reformulations that are more difficult to integrate with an exact decomposition-based solution method, whereas Wasserstein-based sets often yield sample-size-dependent formulations and may cause substantial dimensional growth. In contrast, the adopted moment-based ambiguity set admits an exact conic reformulation of the objective and directly supports the deterministic second-order cone representation of the reliability constraints developed below. Therefore, the main advantage of the present choice lies in its structural compatibility with the joint chance-constrained CBLIP and with the customized OAA, rather than in any claim of universal superiority over alternative DRO paradigms.

The presence of the joint chance constraint (8) makes the model computation intractable. To simplify Equation (8), a natural idea is to decompose it into several independent chance constraints. For convenience in subsequent writing, we define a function

$$\upsilon\left(\boldsymbol{z}_j,y_j\right)=\sum\nolimits_{i\in\mathscr{O}}\zeta_iz_{ij}-y_j.$$

The expected upper bound of this function, i.e., $\mathbb{E}\left[\upsilon\left(\boldsymbol{z}_j,y_j\right)^+\right]$, is closely related to the conic reformulation of independent chance constraints. Here, we define $(\cdot)^+:=\max\{\cdot,0\}$. To examine the properties of this function, we present Lemma 1 and Lemma 2.

Lemma 1. *An upper bound of function* $\mathbb{E}\left[\upsilon\left(\boldsymbol{z}_j,y_j\right)^+\right]$ *is*

$$\pi\left(\boldsymbol{z}_j,y_j\right)=\frac{1}{2}\left(\boldsymbol{z}_j^{\mathrm{T}}\boldsymbol{u}-y_j\right)+\frac{1}{2}\sqrt{\left(\boldsymbol{z}_j^{\mathrm{T}}\boldsymbol{u}-y_j\right)^2+\boldsymbol{z}_j^{\mathrm{T}}\boldsymbol{\Gamma}\boldsymbol{z}_j}.$$

Proof. Please refer to Appendix B of the supplementary material. (Q. E. D.)

Lemma 2. $\pi\left(\boldsymbol{z}_j,y_j\right)$ *is sub-additive.*

Proof. Please refer to Appendix C of the supplementary material. (Q. E. D.)

On the basis of the above lemmas, we propose Proposition 2.

Proposition 2. *The equivalent conical transformation of the independent chance constraint form of chance constraint (8), i.e.,* $\mathbb{P}_G\left(\sum_{i\in\mathscr{O}}\zeta_iz_{ij}\le y_j\right)\ge1-\alpha$, *for all* $j\in\mathscr{D}$, *is as follows*:

$$\boldsymbol{z}_j^{\mathrm{T}}\boldsymbol{u}-y_j+\sqrt{\frac{1-\alpha'}{\alpha'}}\sqrt{\boldsymbol{z}_j^{\mathrm{T}}\boldsymbol{\Gamma}\boldsymbol{z}_j}\le0,\forall j\in\mathscr{D} \tag{16}$$

where $\alpha'=1-\alpha$.

Proof. Please **refer** to Appendix D of the supplementary material. (Q. E. D.)

Based on Proposition 2, we attempt to obtain a conic transformation of the joint chance constraint (8). Note that $\mathbb{P}_G\left(\sum_{i\in\mathscr{O}}\zeta_iz_{ij}\le y_j,\forall j\in\mathscr{D}\right)\ge1-\alpha$ is equivalent to

$$\mathbb{P}_G\left(\bigcup_{j\in\mathscr{D}}\left\{\sum_{i\in\mathscr{O}}\zeta_iz_{ij}-y_j\le0\right\}\right)\ge1-\alpha, \tag{17}$$

Following Chen et al. [68], we decompose (17) into

$$\mathbb{P}_G\left(\sum_{i\in\mathscr{O}}\zeta_iz_{ij}-y_j\le0\right)\ge1-\alpha_j,\forall j\in\mathscr{D}, \tag{18}$$

for computational tractability. By enforcing Bonferroni's inequality on the safety factors of all the constraints in (18), we have $\sum_{j\in\mathscr{D}}\alpha_j\le\alpha$. According to Chen et al. [68] and Nemirovski and Shapiro [69], any feasible solution that satisfies $\sum_{j\in\mathscr{D}}\alpha_j\le\alpha$ and constraint (18) will satisfy constraint (17).

A key aspect of the above transformation is the generation of a new parameter α_j. At this point, accurate selection of the appropriate parameter values is challenging. Intuitively, some scholars (see Nemirovski and Shapiro [69]) choose to directly set $\alpha_j = \alpha / |\mathscr{D}|$, where $|\mathscr{D}|$ represents the cardinality of $\mathscr{D}$, for all $j \in \mathscr{D}$. However, this parameter selection method may lead to an overly conservative solution [70]. To avoid the above shortcomings, we adopt the method of **Theorem 3.1** in Chen et al. [68]. To this end, we define a set $\mathscr{D}_1 := [|\mathscr{D}|]$, a subset $\mathscr{D}_2 \subseteq \mathscr{D}_1$ and a vector $\boldsymbol{p} = \left(p_j\right) > \mathbf{0}$. On the basis of the newly introduced notation, we can develop a mathematical model. According to [70], this method does not affect the feasible region of the problem. Below, Proposition 3 gives the mathematical expression for this model.

Proposition 3. *Define $S(\zeta)$ as the smallest closed convex set containing the support of variable ζ and parameter $\alpha' = 1 - \alpha$. If we have*

$$\Gamma(\boldsymbol{z},\boldsymbol{y},\boldsymbol{p},\mathscr{D}_2)=\min_{(\boldsymbol{a},b_0)}\left\{\min_{\eta\in\mathbb{R}}\left[\eta+\frac{\pi(\boldsymbol{a},b_0+\eta)}{\alpha'}\right]+\frac{1}{\alpha'}\left[\sum_{j\in\mathscr{D}_2}\pi\left(p_j\boldsymbol{z}_j-\boldsymbol{a},p_jy_d-b_0\right)\right]\right\}\leq 0,$$

and $\max_{\zeta\in S(\zeta)}\left(\zeta\boldsymbol{z}_j^{\mathrm{T}}-y_j\right)\leq 0$ *for all* $j\in\mathscr{D}_1\backslash\mathscr{D}_2$*; then, Equation (8) holds.*

Proof. Please refer to Appendix E of the supplementary material. (Q. E. D.)

From an operational perspective, the complex transformation in Proposition 3 serves a highly practical purpose for the decision maker. Instead of rigidly demanding that the entire network never fails (which is mathematically intractable to calculate directly), this proposition safely approximates the system-wide risk. It effectively allocates risk budgets (α_j) to individual BSSs based on their demand distributions, ensuring that even under the worst-case spatial distribution, the overall system's service level strictly adheres to the $1-\alpha$ requirement. However, the existence of $\Gamma(\boldsymbol{z},\boldsymbol{y},\boldsymbol{p},\mathscr{D}_2)\leq 0$ and $\max_{\zeta\in S(\zeta)}\left(\zeta\boldsymbol{z}_j^{\mathrm{T}}-y_j\right)\leq 0$ (for all $j\in\mathscr{D}_1\backslash\mathscr{D}_2$) still makes the model computationally intractable. To further simplify it, we introduce two auxiliary variables (i.e., c_0 and c_j). The condition $\Gamma(\boldsymbol{z},\boldsymbol{y},\boldsymbol{p},\mathscr{D}_2)\leq 0$ is exactly equivalent to the existence of $b_0, c_0, \in \mathbb{R}$, $\boldsymbol{a} = (a_i) \in \mathbb{R}^{|\mathscr{O}|}$, and $\boldsymbol{c} = \left(c_j\right) \in \mathbb{R}^{|\mathscr{D}_2|}$ such that the following linear and conic relationships hold:

$$c_0+\frac{1}{\alpha'}\sum_{j\in\mathscr{D}_2}c_j\leq 0 \tag{19}$$

$$UB_{1-\alpha'}[\pi(\boldsymbol{a},b_0+\eta)]\leq c_0\ \forall j\in\mathscr{D}_2 \tag{20}$$

$$\pi\left(p_j\boldsymbol{z}_j-\boldsymbol{a},p_jy_d-b_0\right)\leq c_j\ \forall j\in\mathscr{D}_2. \tag{21}$$

Moreover, to simplify the robust counterpart (i.e., $\max_{\zeta\in S(\zeta)}\left(\zeta\boldsymbol{z}_j^{\mathrm{T}}-y_j\right)\leq 0$), we can follow **Theorem 3(c)** proposed by Chen and Sim [71] and reformulate it to

$$\boldsymbol{z}_j^{\mathrm{T}}\boldsymbol{u}-y_j+\varepsilon_2\sqrt{\boldsymbol{z}_j^{\mathrm{T}}\boldsymbol{\Gamma}\boldsymbol{z}_j}\leq 0\ \forall j\in\mathscr{D}_1\backslash\mathscr{D}_2. \tag{22}$$

After the above transformation, **M2** can be equivalently converted into **M3**.

M3:

$$\min\sum_{j\in\mathscr{D}}\left(c_jx_j+h_jy_j\right)+\varepsilon_1\theta+\boldsymbol{\mu}^{\mathrm{T}}\boldsymbol{m} \tag{23}$$

s.t. (2), (3), (4), (6), (7), (9), (10), (13), (14), (19), (20), (21), (22).

Now, we examine **M3** obtained from the current reconstruction. We find that under certain circumstances, **M3** possesses some desirable properties, which are specifically stated in Lemma 3 and Proposition 4.

Lemma 3. *Equations (19)–(21) dominate Equation (16).*

Proof. Please refer to Appendix F of the supplementary material. (Q. E. D.)

Proposition 4. *If we set*

$$\varepsilon_2\leq\sqrt{(1-\alpha')/\alpha'}, \tag{24}$$

then we have $\mathscr{D}_2 = \varnothing$; i.e., Equations (19)–(21) are redundant.

Proof. Please refer to Appendix G of the supplementary material. (Q. E. D.)

Based on the lemma and proposition above, we finally convert **M3** into the following **M4**.

M4:

$$\min\sum_{j\in\mathscr{D}}\left(c_jx_j+h_jy_j\right)+\varepsilon_1\theta+\boldsymbol{\mu}^{\mathrm{T}}\boldsymbol{m} \tag{25}$$

s.t. (2), (3), (4), (6), (7), (9), (10), (13), (14), (22), (24).

After a series of model transformations, **M4** is a parametric SOCP. This lays the foundation for us to construct an OAA to efficiently solve the model.

5. Algorithm design

After the reformulation in Section 4, the original problem is reduced to the tractable model **M4**. Therefore, the role of Section 5 is not to solve the original model **M1** directly but to design an exact solution framework for **M4**. While several advanced decomposition techniques, such as Benders decomposition, CCG, and Lagrangian relaxation, are widely used in optimization, they present structural limitations for **M4**. The CCG is strictly tailored for min-max-min structures, whereas our framework has been analytically reduced to a single-level SOCP. Lagrangian relaxation struggles to recover exact primal feasibility for nonlinear joint chance constraints. Furthermore, because **M4** is a nonlinear SOCP, the standard Benders decomposition is inapplicable. While generalized Benders decomposition could theoretically be applied, OAA is substantially superior for convex mixed-integer nonlinear programming problems (MINLPs) because it leverages the gradients of nonlinear functions to construct tighter linear relaxations in the master problem, leading to faster convergence. Thus, we design a customized OAA to solve **M4** in Section 4.

The OAA is a cutting plane algorithm designed by Duran and Grossmann [72] to solve MINLPs (e.g., the SOCP we develop). Typically, these problems involve both discrete decision variables (e.g., integer/binary decisions such as whether to construct a BSS) and continuous decision variables (e.g., flow volume), with nonlinear relationships in the objective function and/or constraints. The fundamental idea of OAA is to approximate the nonlinear feasible region from the outside using a series of linear constraints. By solving a sequence of simpler MILP master problems and nonlinear programming (NLP) subproblems, OAA converges toward the optimal MINLP solution.

The core computational process of the OAA involves the following stages. First, before the first iteration of OAA begins, a solution of the original MINLP should be supplied to the master problem to initialize the OAA. The subproblem is subsequently solved with all integer variables held fixed, which simultaneously yields an upper bound of the MINLP. Taking advantage of the convex nature of the nonlinear terms in the MINLP, these terms are linearized to formulate the master problem. Next, the master problem is solved via a collection of valid cuts derived from the subproblem, the solution of which also supplies a lower bound for the MINLP. Finally, the master problem and subproblems are solved in an alternating iterative manner. This process gradually improves the approximation of the nonlinear terms in the master problem and reduces the gap between the upper and lower bounds as the number of iterations increases. For further details on this algorithm, readers may refer to [72, 73].

In Bonami et al. [73], the authors demonstrated that the global optimal solution for convex MINLP (C-MINLP) can be obtained via this algorithm. If the continuous relaxation of an MINLP is a convex model, then this MINLP is called a C-MINLP. Fortunately, we can prove that **M4** is a C-MINLP and use Proposition 5 to ensure algorithm optimality and applicability. Since all the terms in **M4** except for Equations (14) and (22) are linear terms, we consider only these two equations in Proposition 5.

Proposition 5. *Model **M4** is a C-MINLP because of the continuous relaxation of Equations (14) and (22), i.e.,*

$$f_1(\boldsymbol{m},\theta)=\sqrt{\boldsymbol{m}^{\mathrm{T}}\boldsymbol{\Sigma}\boldsymbol{m}}-\theta \text{ and}$$

$$f_2\left(\boldsymbol{z}_j,y_j\right)=\boldsymbol{z}_j^{\mathrm{T}}\boldsymbol{u}-y_j+\varepsilon_2\sqrt{\boldsymbol{z}_j^{\mathrm{T}}\boldsymbol{\Gamma}\boldsymbol{z}_j}$$

are both convex, and the other constraints are linear.

Proof. Please refer to Appendix H of the supplementary material. (Q. E. D.)

Remark 3. In terms of computational complexity, the worst-case complexity of **M4** is inherently NP-hard. The practical time complexity of OAA relies on the total number of iterations and the complexity of the MILP master problem solved per iteration. However, since **M4** is proven to be a C-MINLP, the OAA guarantees convergence to the global optimum within a finite number of iterations.

5.1. Initialization of OAA

Before performing the first iteration of the algorithm, we need to input a feasible solution to start the algorithm. Let $\widetilde{x}_j^t$ and $\widetilde{y}_j^t$ be the binary and integer variables that are input into the subproblem in the tth iteration. Before the algorithm iteration begins, the decision variables input to the subproblem are denoted as $\widetilde{x}_j^1$ and $\widetilde{y}_j^1$. We assume that each candidate node constructs a BSS, i.e., $\widetilde{x}_j^1=1$ for all $j\in\mathscr{D}$. Afterward, following Equation (2), we can directly set $y_j=\overline{y}_j$ for all $j\in\mathscr{D}$.

5.2. Subproblem of OAA

When a subproblem is solved, all integer variables need to be fixed. At the tth iteration, the expression for the subproblem to be solved (i.e., model **SP**) is as follows. Note that at this point, integer variables $\left(\widetilde{x}_j^t,\widetilde{y}_j^t\right)^{\mathrm{T}}$ are known. Notably, to maintain the completeness of the model, we repeat some constraints in the **SP**.

SP:

$$\min_{(\boldsymbol{z},\boldsymbol{m},\theta)}\sum_{j\in\mathscr{D}}\left(c_j\widetilde{x}_j^t+h_j\widetilde{y}_j^t\right)+\varepsilon_1\theta+\boldsymbol{\mu}^{\mathrm{T}}\boldsymbol{m} \tag{26}$$

$$s.t.\sum_{j\in\mathscr{D}}z_{ij}=1\ \forall i\in\mathscr{O} \tag{27}$$

$$z_{ij}\le\widetilde{x}_j^t\ \forall i\in\mathscr{O},j\in\mathscr{D} \tag{28}$$

$$\boldsymbol{z}\in[0,1]^{|\mathscr{O}|\times|\mathscr{D}|} \tag{29}$$

$$m_i=\sum_{j\in\mathscr{D}}\left(\beta d_{ij}+\gamma_j\right)z_{ij}\ \forall i\in\mathscr{O} \tag{30}$$

$$\left\|\boldsymbol{\Sigma}^{1/2}\boldsymbol{m}\right\|\le\theta \tag{31}$$

$$\boldsymbol{z}_j^{\mathrm{T}}\boldsymbol{u}-\widetilde{y}_j^t+\varepsilon_2\sqrt{\boldsymbol{z}_j^{\mathrm{T}}\boldsymbol{\Gamma}\boldsymbol{z}_j}\le 0\ \forall j\in\mathscr{D} \tag{32}$$

$$\theta\in\mathbb{R}_+ \tag{33}$$

$$\boldsymbol{m}\in\mathbb{R}_+^{|\mathscr{O}|}. \tag{34}$$

Note that in Equation (32), the range of j has been changed from $j\in\mathscr{D}_1\backslash\mathscr{D}_2$ to $j\in\mathscr{D}$ because of Lemma 3. For ease of description, we let $\widetilde{z}_{ij}^t$, $\widetilde{\boldsymbol{m}}^t=\left(\widetilde{m}_i^t\right)$ and $\widetilde{\theta}^t$ be the continuous variables that are solved by the subproblem in the tth iteration.

5.3. Master problem of OAA

When this MILP is solved, the optimal values for the decision variables obtained from the subproblem (including $\widetilde{z}_{ij}^t$, $\widetilde{\boldsymbol{m}}^t=\left(\widetilde{m}_i^t\right)$ and $\widetilde{\theta}^t$) need to be used as inputs. Before the mathematical expression for the master problem is given, we relax the nonlinear constraints in the original model. The relaxed constraints are also called *OA cuts*.

Proposition 6. *The valid linear OA cuts (i.e., relaxed constraints) of **M4** associated with the t^{th} iteration are as follows:*

$$\boldsymbol{m}^{\mathrm{T}}\boldsymbol{\Sigma}\widetilde{\boldsymbol{m}}^t-\theta\widetilde{\theta}^t\le 0 \tag{35}$$

$$\left(\boldsymbol{z}_j^{\mathrm{T}}\boldsymbol{u}-y_j\right)\sqrt{\left(\widetilde{\boldsymbol{z}}_j^t\right)^{\mathrm{T}}\boldsymbol{\Gamma}\widetilde{\boldsymbol{z}}_j^t}+\varepsilon_2\boldsymbol{z}_j^{\mathrm{T}}\boldsymbol{\Gamma}\widetilde{\boldsymbol{z}}_j^t\le 0\ \forall j\in\mathscr{D}. \tag{36}$$

Proof. Please refer to Appendix I of the supplementary material. (Q. E. D.)

On the basis of Proposition 6, we present the expression for the master problem as follows. Here, we define the maximum number of iterations of the algorithm as T and set $\mathscr{T}:=[T]$, where $t\in\mathscr{T}$. Parameters UB and LB represent the upper bound and lower bound of the model, respectively; parameter ι is a small positive number. They are updated as the algorithm iterates. To maintain the completeness of the model, we repeat some constraints here. Following Fletcher and Leyffer [74], we introduce constraint (39). The pseudocode of the OAA is shown in **Algorithm 1**.

Algorithm 1

Initialization: (i) $\left(\widetilde{\boldsymbol{x}}^1,\widetilde{\boldsymbol{y}}^1\right)^{\mathrm{T}}$: initial value of binary/integer decision variable.
(ii) $\mathscr{T}$: maximum algorithm iteration number.
(iii) UB^1 and UL^1: upper/lower bound, equal to $+\infty/-\infty$.
(iv) ι: optimality gap.
Procedure:
Set $t=1$. Calculate $\left(\widetilde{\boldsymbol{x}}^1,\widetilde{\boldsymbol{y}}^1\right)^{\mathrm{T}}$ based on Section 5.1.
For $t=1:\mathscr{T}$
  Solve **SP** via a commercial solver (e.g., CPLEX) with $\left(\widetilde{\boldsymbol{x}}^t,\widetilde{\boldsymbol{y}}^t\right)^{\mathrm{T}}$. Obtain subproblem objective function value z_{sub}^t and $\left(\widetilde{\boldsymbol{z}}^t,\widetilde{\boldsymbol{m}}^t,\widetilde{\theta}^t\right)^{\mathrm{T}}$. If $z_{\text{sub}}^t<UB^t$, update the upper bound.
  Add cuts (41) to (42) into **MP** according to $\left(\widetilde{\boldsymbol{z}}^t,\widetilde{\boldsymbol{m}}^t,\widetilde{\theta}^t\right)^{\mathrm{T}}$.
  Solve **MP** via a commercial solver with $\left(\widetilde{\boldsymbol{z}}^t,\widetilde{\boldsymbol{m}}^t,\widetilde{\theta}^t\right)^{\mathrm{T}}$ to obtain $\left(\widetilde{\boldsymbol{x}}^t,\widetilde{\boldsymbol{y}}^t\right)^{\mathrm{T}}$.
  If MP is infeasible **then**
    Break and report the optimal solution $\left(\widetilde{\boldsymbol{z}}^t,\widetilde{\boldsymbol{m}}^t,\widetilde{\theta}^t,\widetilde{\boldsymbol{x}}^t,\widetilde{\boldsymbol{y}}^t\right)^{\mathrm{T}}$.
  End if
  Update $\left(\widetilde{\boldsymbol{x}}^t,\widetilde{\boldsymbol{y}}^t\right)^{\mathrm{T}}$ and LB^t based on the optimal objective function value of **MP**.
End for

MP:

$$\min_{(\boldsymbol{x},\boldsymbol{y},\boldsymbol{z},\boldsymbol{m},\theta,\chi)}\chi \tag{37}$$

$$s.t.\ \chi\ge\sum_{j\in\mathscr{D}}\left(c_jx_j+h_jy_j\right)+\varepsilon_1\theta+\boldsymbol{\mu}^{\mathrm{T}}\boldsymbol{m} \tag{38}$$

$$\chi\le UB-\iota \tag{39}$$

$$\chi \geq LB \tag{40}$$

$$\boldsymbol{m}^{\mathrm{T}}\boldsymbol{\Sigma}\widetilde{\boldsymbol{m}}^{t} - \theta\widetilde{\theta}^{t} \leq 0 \ \forall t \in \mathscr{T} \tag{41}$$

$$\left(\mathbf{z}_j^{\mathrm{T}}\boldsymbol{u} - y_j\right)\sqrt{\left(\widetilde{\mathbf{z}}_j^t\right)^{\mathrm{T}}\boldsymbol{\Gamma}\widetilde{\mathbf{z}}_j^t} + \varepsilon_2\mathbf{z}_j^{\mathrm{T}}\boldsymbol{\Gamma}\widetilde{\mathbf{z}}_j^t \leq 0 \ \forall j \in \mathscr{D}, t \in \mathscr{T} \tag{42}$$

$$\sum_{j\in\mathscr{D}} z_{ij} = 1 \ \forall i \in \mathscr{O} \tag{43}$$

$$z_{ij} \leq x_j \ \forall i \in \mathscr{O}, j \in \mathscr{D} \tag{44}$$

$$m_i = \sum_{j\in\mathscr{D}}\left(\beta d_{ij} + \gamma_j\right)z_{ij} \ \forall i \in \mathscr{O} \tag{45}$$

$$y_j \leq \bar{y}_j x_j \ \forall j \in \mathscr{D} \tag{46}$$

$$\boldsymbol{x} \in \{0,1\}^{|\mathscr{D}|} \tag{47}$$

$$\boldsymbol{y} \in \mathbb{Z}_+^{|\mathscr{D}|} \tag{48}$$

$$\boldsymbol{z} \in [0,1]^{|\mathscr{O}|\times|\mathscr{D}|} \tag{49}$$

$$\boldsymbol{m} \in \mathbb{R}_+^{|\mathscr{O}|} \tag{50}$$

$$\theta \in \mathbb{R}_+. \tag{51}$$

6. Numerical experiment

In this section, numerical experiments are used to verify the effectiveness of OAA. First, Section 6.1 introduces the basis for our parameter settings. Section 6.2 presents experiments to assess algorithm performance. Section 6.3 presents a sensitivity analysis. Finally, an out-of-sample analysis is presented in Section 6.4 and Appendix N to validate the effectiveness of our model and compare our method with traditional stochastic programming and robust optimization methods. Owing to space limitations, some management insights are detailed in Appendix K of the supplementary material.

6.1. Parameter setting

Due to the strict confidentiality of commercial operational data from CEV operating companies (such as large-scale ride-sourcing fleets), the parameters for our numerical experiments are primarily adopted from established literature (i.e., [3], [57], and [75]) to ensure the reproducibility of our results. While these values serve as a proxy for real-world scenarios, our model is fundamentally data-agnostic. In practical applications, the proposed DRO framework can be directly driven by actual operational moments (mean and covariance) once real-world fleet datasets become available to the decision makers of the CEV operating companies. On the basis of the collection of parameters in Guo et al. [3] and a literature review, we summarize the parameter values used in this paper and their sources in Table 1. Two covariance matrices, i.e., $\boldsymbol{\Sigma}$ and $\boldsymbol{\Gamma}$, can be calculated from the correlation coefficient and variance of the random variables.

To estimate the radius parameter $\varepsilon_1 \in \mathbb{R}_{++}$ in Equation (11), we adopt the technique proposed by Delage and Ye [66]. For each demand generation node, we generate $M = 1000$ independent scenarios. Based on these scenarios, we calculate $\boldsymbol{\mu}_0 = \frac{1}{1000}\sum_{i=1}^{1000}\widehat{\boldsymbol{\xi}}_i$ and $\widehat{\boldsymbol{\Sigma}}_0$. Afterward, we set $\delta = 0.05$ and use $\max_{i\in\{1,2,\cdots,1000\}}\left(\widehat{\boldsymbol{\xi}}_i - \boldsymbol{\mu}_0\right)^{\mathrm{T}}\widehat{\boldsymbol{\Sigma}}_0^{-1}\left(\widehat{\boldsymbol{\xi}}_i - \boldsymbol{\mu}_0\right)$ to determine the value of parameter R^2. Finally, we calculate the parameter $\varepsilon_1 = \left(R^2/1000\right)\left[2 + \sqrt{2\ln(1/\delta)}\right]^2$.

With respect to transportation networks, we use the classic Nguyen–Dupius network and Sioux Falls network as our research subjects. In transportation research, standardized test networks are essential tools. They allow scholars to construct, evaluate, and verify various methods for traffic simulation, route assignment, and network modeling. Among these, the Nguyen–Dupuis network [76] and the Sioux Falls network [77] are prominent and frequently used benchmarks. They play distinct roles because of their different scales and origins: The first is a compact, deliberately constructed model ideal for testing core methodologies, whereas the second is a medium-scale network based on actual city data, which is used primarily to assess how algorithms perform in realistic settings. Furthermore, regarding spatial topology, the nodes in the selected classical networks (i.e., Nguyen-Dupuis and Sioux Falls) represent macroscopic traffic analysis zones or distinct urban districts rather than microscopic street intersections. This spatial aggregation implies that a network size of up to 55 demand nodes (as tested in our scalability analysis) practically reflects the strategic planning scope of a large metropolitan area.

Table 1
Parameter setting scheme.

Parameter	Value	Source
α'	0.95	
β	0.55 (Unit: \$/km)	[3] and [57]
c_j	109 (Unit: \$/day)	[3]
h_j	1.58 (Unit: \$/day)	[75]
γ_j	0.5 (Unit: \$/day)	
$\bar{y}_j$	U[30, 45]	[3]
ξ_i	Mean $\mu_i \in$ U[0.1, 15] and standard deviation $\sigma_i \in$ U[0.5, 2]	
$\boldsymbol{\Sigma}$	Correlation coefficient $\rho_{ij}^{\xi} = 0.1, \forall i \neq j$; $\rho_{ij} = 1, \forall i \neq j$	
ζ_i	Mean $u_i \in$ U[0.1, 10] and standard deviation $\tau_i \in$ U[0.5, 3]	
$\boldsymbol{\Gamma}$	Correlation coefficient $\rho_{ij}^{\zeta} = 0.1, \forall i \neq j$; $\rho_{ij} = 1, \forall i \neq j$	

All the models are implemented in GAMSPy (https://gamspy.readthedocs.io/en/latest/). The deterministic model and the master/subproblem pair embedded in the proposed OAA are solved using CPLEX within the GAMS environment, whereas commercial solver DICOPT is used as the benchmark exact MINLP solver in the comparative experiment. Unless otherwise stated, the default solver settings are adopted. For the comparative experiments reported in Section 6.2.2, a time limit of 3600 s is imposed for each run. The stopping condition of the proposed OAA follows **Algorithm 1** and is governed by the prescribed maximum number of iterations and the optimality gap. All the programs are executed on a Lenovo computer equipped with an Intel (R) Core™ Ultra 5-228V (2.10 GHz) processor and 32 GB of RAM.

6.2. Algorithm performance test

We first conduct numerical experiments on the Nguyen–Dupuis network, and the network structure is shown in Fig. 2. There are 13 nodes in this network, of which nodes 2, 5, 7, 10, and 13 are selected as the BSS candidate construction locations. The distances between nodes (i.e., d_{ij}) are derived from Guo et al. [57]. We present two analyses to

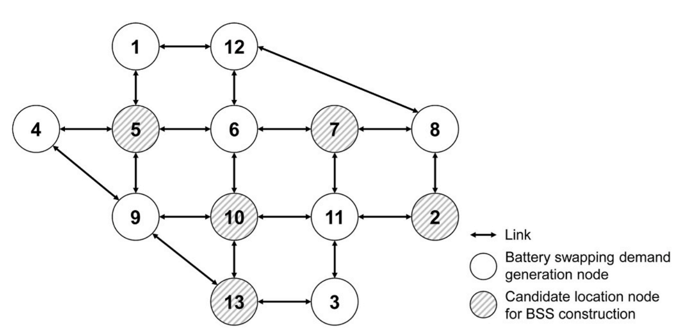

Fig. 2. Nguyen–Dupuis network.

verify the effectiveness of the model and algorithm. First, we compare the optimal solutions obtained by the deterministic model and the DRO model. Here, the parameters input to the deterministic model are derived from Table 1, and various uncertain demands are replaced by the mean values generated by the rules described in Table 1. Second, we conduct a computational performance comparison with commercial solver DICOPT.

6.2.1. Analysis of the impact of uncertainty on the optimal solution

First, we present the mathematical expression for the deterministic model. Since the model does not contain any uncertain parameters (i.e., random variables), it is directly written as a single-stage model. The mathematical expression for the above model is as follows. Notably, $\overline{\xi}_i$ and $\overline{\zeta}_i$ in the **DM** are no longer random variables but rather means (i.e., parameters) calculated in the manner described in Table 1. To maintain the completeness of the model, we repeat some constraints in the **DM**.

DM:

$$\min_{(\boldsymbol{x},\boldsymbol{y},\boldsymbol{z})}\sum_{j\in\mathscr{D}}\left(c_jx_j+h_jy_j\right)+\sum_{i\in\mathscr{O}}\left[\overline{\xi}_i\sum_{j\in\mathscr{D}}\left(\beta d_{ij}+\gamma_j\right)z_{ij}\right] \tag{52}$$

$$s.t.\ y_j\le\overline{y}_jx_j\ \forall j\in\mathscr{D} \tag{53}$$

$$\sum_{j\in\mathscr{D}}z_{ij}=1\ \forall i\in\mathscr{O} \tag{54}$$

$$z_{ij}\le x_j\ \forall i\in\mathscr{O},j\in\mathscr{D} \tag{55}$$

$$\sum_{i\in\mathscr{O}}\overline{\zeta}_iz_{ij}\le y_j\ \forall j\in\mathscr{D} \tag{56}$$

$$\boldsymbol{x}\in\{0,1\}^{|\mathscr{D}|} \tag{57}$$

$$\boldsymbol{y}\in\mathbb{Z}_+^{|\mathscr{D}|} \tag{58}$$

$$\boldsymbol{z}\in[0,1]^{|\mathscr{O}|\times|\mathscr{D}|} \tag{59}$$

$$\boldsymbol{z}\in\mathbb{R}_+^{|\mathscr{O}|\times|\mathscr{D}|}. \tag{60}$$

Note that the **DM** is an MILP with a limited problem scale and can be solved directly via a commercial solver (e.g., CPLEX in GAMS). To evaluate the trade-off between cost efficiency and system resilience, we solve the **DM** and our two-stage DRO. Table 2 and Fig. 3 present a comparative analysis of the optimal solutions derived from the deterministic model and the DRO model.

While both approaches reach a consensus on the topological configuration by selecting nodes 5 and 7 as the optimal locations for BSS construction (i.e., $x_5=1$, $x_7=1$), the resulting operational strategies and system costs diverge significantly. The deterministic model, which assumes perfect demand information, yields a total system cost of 309.98. In contrast, the DRO model results in an objective value of 589.52. This represents an approximately 90.2% increase in cost, quantifying the *price of robustness*—the necessary financial premium required to ensure solution feasibility under worst-case probability distributions. Although the DRO framework increases the total cost by approximately 90%, this price of robustness is rational and economically acceptable in the context of CEV fleets. For commercial operations such as ride-sourcing or urban delivery, service reliability is the lifeline of profitability. A battery shortage at a BSS directly leads to ground vehicles, incurring severe penalty costs that include lost daily revenue, service level agreement violations, and driver compensation. Conservatively estimating this outage penalty at $50 per unmet swap demand, the daily DRO investment premium of approximately $280 equates to the penalty cost of merely 5 to 6 vehicle outages. Because this premium primarily funds an expanded battery inventory buffer rather than redundant facility construction, it effectively functions as a highly cost-effective insurance policy. It shields the CEV operating company from catastrophic systemic disruptions across the city-wide network, validating the practical necessity of the DRO approach.

Table 2
Optimal solutions obtained by the deterministic model and DRO model.

$j\in\mathscr{D}$	Deterministic model (Objective value = 309.98)			DRO model (Objective value = 589.52)		
	x_j	y_j	z_{ij}	x_j	y_j	z_{ij}
2	0	0	N/A	0	0	N/A
5	1	24	[1.0, 0, 1.0, 0, 0, 1.0, 0, 0.15]	1	42	[0.6, 0.6, 0.6, 0.6, 0.6, 0.6, 0.6]
7	1	25	[0, 1.0, 0, 1.0, 1.0, 0, 1.0, 0.85]	1	31	[0.4, 0.4, 0.4, 0.4, 0.4, 0.4, 0.4]
10	0	0	N/A	0	0	N/A
13	0	0	N/A	0	0	N/A

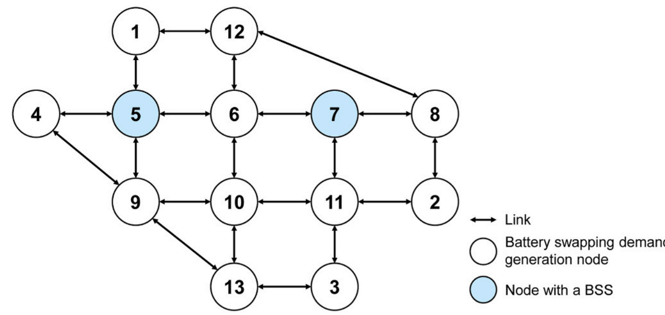

Fig. 3. BSS location selection results.

The conservative nature of the DRO model is explicitly reflected in the battery inventory level decisions (i.e., y_j) and demand allocation patterns (i.e., z_{ij}). To buffer against demand ambiguity, the robust solution significantly expands the onsite battery inventory; for example, the battery capacity at node 5 increases from 24 units in the deterministic solution to 42 units in the DRO solution, whereas node 7 increases from 25 to 31 units. Furthermore, the demand satisfaction strategy shifts from a polarized approach to a diversified approach. Unlike the deterministic model, which employs "greedy" binary-like assignments (e.g., assigning specific demand nodes exclusively to one station to minimize distance), the DRO model distributes the demand from the eight generation nodes more evenly across the two BSSs (indicated by the z_{ij} vectors converging toward proportions of 0.6 and 0.4). By avoiding over-reliance on a single station for specific demand sources, the DRO framework effectively hedges against uncertainty, ensuring that the network remains resilient even when facing simultaneous worst-case demand scenarios across different regions.

6.2.2. Computational performance comparison with DICOPT

To evaluate the computational effectiveness of the proposed OAA beyond standalone convergence behavior, we benchmark it against commercial solver DICOPT, which is employed in this paper as a representative state-of-the-art exact MINLP solver. This comparison is intended to assess whether the customized algorithm offers a tangible computational advantage for the same class of MINLPs arising from the reformulated model. We conduct numerical experiments across ten groups of test instances, expanding from small-scale scenarios (e.g., $|\mathscr{O}|=10$, $|\mathscr{D}|=5$) to larger-scale networks (e.g., $|\mathscr{O}|=55$, $|\mathscr{D}|=50$). To ensure a fair comparison, both methods are tested under the same hardware environment and the same time limit of 3600 s for each run. The detailed results are reported in Table 3.

The computational performance of DICOPT decreases exponentially with increasing problem size. While it solves the smallest instance slightly faster than our algorithm does (averaging 0.43 s versus 0.54 s), its computational burden increases rapidly. In Scenario 5 (i.e., $|\mathscr{O}|=30$,

Table 3
Computational time and number of iterations for problems of different sizes.

No.	$\lvert\mathscr{O}\rvert$	$\lvert\mathscr{D}\rvert$	Computational time (s) of DICOPT			Computational time (s) of OAA			Number of iterations of OAA	
			Min	Ave	Max	Min	Ave	Max	Min	Max
1	10	5	0.27	0.43	0.68	0.51	0.54	0.64	3	3
2	15	10	1.46	3.03	5.63	0.73	0.94	1.11	4	6
3	20	15	4.56	21.48	35.44	1.42	1.77	2.21	8	12
4	25	20	47.15	353.37	726.14	1.91	2.63	3.62	10	13
5	30	25	899.66	1635.43	2962.03	2.03	3.55	3.97	7	14
6	35	30	>3600	>3600	>3600	3.70	4.24	5.30	9	18
7	40	35	>3600	>3600	>3600	3.68	7.19	17.77	10	18
8	45	40	>3600	>3600	>3600	5.01	8.35	14.37	14	24
9	50	45	>3600	>3600	>3600	6.42	9.92	23.51	11	22
10	55	50	>3600	>3600	>3600	9.07	13.51	23.31	19	27

$|\mathscr{D}| = 25$), DICOPT requires an average of 1635.43 s, and for all subsequent larger scenarios (Scenarios 6–10), the commercial solver completely fails to converge within the 3600-s time limit. This failure highlights the severe computational intractability of high-dimensional joint chance constraints when they are processed by generic commercial algorithms. In stark contrast, our customized OAA demonstrates exceptional scalability. By precisely exploiting the convex structure of the reformulated SOCP to generate tight valid cuts, our algorithm reliably solves the most demanding instance (Scenario 10) in an average of 13.51 s, with the iteration count stably bounded under 27 iterations. This empirical benchmark unequivocally validates the necessity and computational superiority of our tailored algorithm in supporting large-scale network planning.

In parallel with time efficiency, the convergence behavior of the algorithm is stable and robust. The right-hand section of Table 3 reveals that the number of iterations required to reach optimality increases moderately relative to the problem size. The iteration count ranges from a minimum of 3 in simple cases to a maximum of 27 in the most demanding instances. The data indicate that the cut-generation mechanism within the algorithm is highly effective; it efficiently narrows the search space of the uncertainty set, ensuring that the global optimal solution is attained with a limited number of iterations, even as the network scale increases significantly.

6.3. Sensitivity analysis

To rigorously validate the proposed model and assess the stability of the obtained solutions, a comprehensive sensitivity analysis is conducted to observe how variations in key parameters influence the model's output. These sensitivity parameters are carefully selected to bridge mathematical modeling with practical operational dynamics: the ambiguity radius reflects market data volatility; the unit transportation cost captures urban congestion and varying energy prices; the inventory limits simulate physical land use constraints in dense urban centers; the expected demand tracks the long-term adoption growth of CEV fleets; and the BSS construction cost evaluates the network's adaptability to fluctuating infrastructure capital expenditures.

Numerical experiments are performed via the Sioux Falls network (Fig. 4), a quintessential benchmark dataset widely utilized in the transportation and logistics literature for evaluating network design and traffic assignment algorithms. This network serves as a realistic proxy for an urban transportation system, featuring a topology consisting of 28 nodes and 76 directed links. In the context of our experimental design, we have strategically designated nodes 6 through 13 as candidate locations for the construction of the BSS, while the remaining nodes are characterized as battery swapping demand generation nodes. We refer to Table 3 to set the parameters. The distance between two nodes is set according to [78].

6.3.1. Sensitivity analysis of the radius of the ambiguity set

In this subsection, the impact of the radius of the ambiguity set $\mathscr{G}$, denoted as ε_2, on the optimal solution of the proposed DRO model is investigated. The parameter ε_2 serves as a proxy for the level of distributional uncertainty; a larger radius implies that the decision-maker

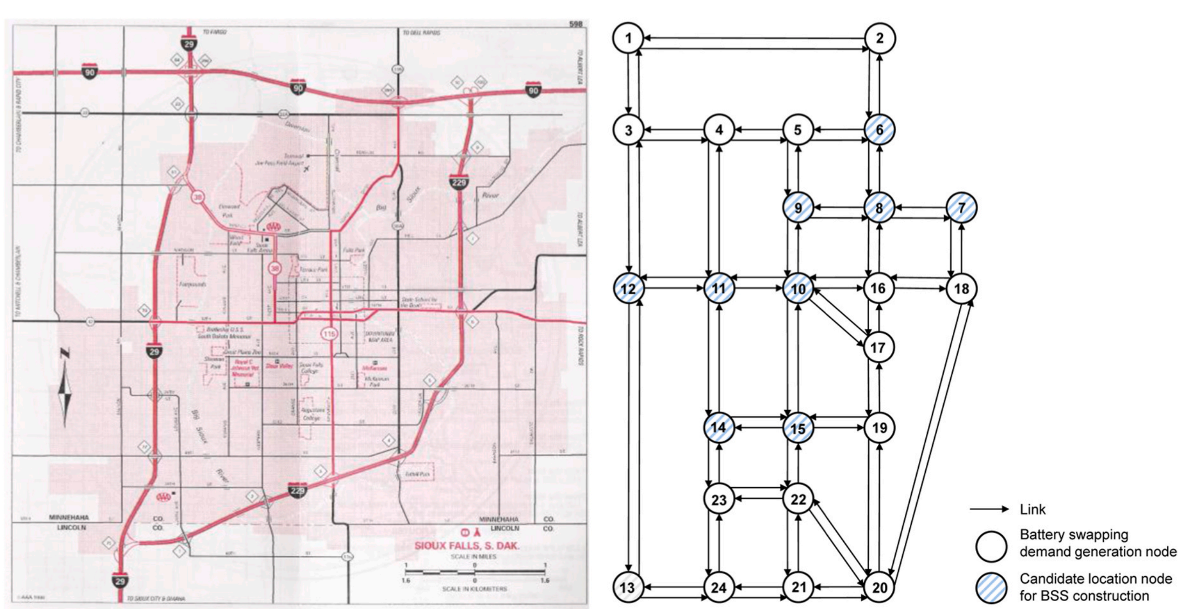

Fig. 4. Sioux Falls network.

considers a wider range of potential worst-case distributions, thereby requiring a more robust solution. As presented in Table 4 and Fig. 5, we vary the radius ε_2 from 1.0 to 4.3 in increments of 0.3. A distinct monotonic upward trend is observed in the objective function value as the radius expands. Specifically, the value increases from 3442.08 at $\varepsilon_2 = 1.0$ to 3543.86 at $\varepsilon_2 = 4.3$. This phenomenon aligns with the theoretical underpinnings of robust optimization: as the uncertainty set increases, the DRO model has more freedom to select a distribution that is detrimental to system performance. Thus, the transportation system must incur a higher cost—often referred to as the price of robustness—to guarantee service levels under these increasingly severe worst-case scenarios.

Interestingly, despite the rising costs and increasing uncertainty, the optimal configuration of BSS locations is remarkably stable. Throughout the entire range of the sensitivity analysis, the set of selected nodes for BSS construction remains invariant and is consistently identified as nodes 6, 7, 12, 14, and 15. This topological consistency suggests that location decisions are structurally robust and are not hypersensitive to fluctuations in the magnitude of distributional ambiguity. For decision makers, this is a highly favorable property, as it indicates that the strategic facility location plan remains valid even if the estimation of the uncertainty level is not perfectly precise. However, while the locations remain static, the model adapts to higher uncertainty by adjusting the operational capacity. As shown in the final two columns of Table 4, the radius ε_2 and the required battery inventory are clearly positively correlated. The total system battery inventory increases from 85 units to 140 units as the radius increases. By analyzing the specific nodes, we observe that the inventory levels at each selected BSS (e.g., Node 7 rising from 18 to 36 and Node 14 rising from 9 to 18) increase to create a larger buffer against demand fluctuations. These findings indicate that the proposed model primarily manages increased risk not by relocating facilities but by densifying the resources at key hubs to absorb the potential shocks caused by extreme demand distributions.

6.3.2. Sensitivity analysis of the unit transportation cost

This subsection explores the sensitivity of the optimal solution to variations in the unit transportation cost (β), a parameter that encapsulates the operational costs incurred by CEVs, such as electricity consumption and the value of travel time. In this analysis, the unit transportation cost is adjusted from 50% to 300% of the baseline value to simulate diverse economic scenarios, ranging from highly efficient travel conditions to environments with severe congestion or high energy prices. As detailed in Fig. 6 and Table 5, the objective function value sharply and monotonically increases in response to rising transportation costs, increasing from 2125.22 in the 50% scenario to 9058.40 in the 300% scenario.

More importantly, the variation in unit transportation costs triggers a distinct structural evolution in the optimal BSS location. The results reveal a fundamental trade-off between the fixed costs of establishing facilities (i.e., BSSs) and the variable costs of transportation. In the low-cost regimes (50% and 60%), the model adopts a centralized strategy, selecting a minimal set of four nodes (6, 7, 13, and 15). Under these conditions, the relatively low cost of travel allows CEV drivers to cover longer distances to reach a BSS without incurring prohibitive penalties, thereby allowing the transportation system to economize construction costs. However, as the unit transportation cost increases, this dynamic inverts. In the high-cost scenarios (250% and 300%), the solution shifts toward a decentralized, denser configuration, expanding the network to six nodes (adding nodes 12 and 14 to the set). This spatial expansion demonstrates that when travel becomes expensive, the optimal strategy is to bring the service closer to demand by increasing the number of facilities, effectively substituting highly variable CEV transportation costs with fixed investment costs.

Finally, with respect to the inventory levels, the system displays a

Table 4
Optimal solutions obtained under different radii of the ambiguity set $\mathscr{G}$

No.	Radius (ε_2)	Objective function value	Location of BSS	System battery inventory level	Battery inventory levels at each BSS
1	1.0	3442.08	6, 7, 12, 14, 15	85	10, 18, 20, 9, 28
2	1.3	3449.35	6, 7, 12, 14, 15	90	12, 19, 20, 10, 29
3	1.6	3458.30	6, 7, 12, 14, 15	96	13, 21, 21, 11, 30
4	1.9	3465.97	6, 7, 12, 14, 15	101	14, 22, 22, 12, 31
5	2.2	3472.07	6, 7, 12, 14, 15	105	15, 23, 23, 12, 32
6	2.5	3479.76	6, 7, 12, 14, 15	110	16, 24, 24, 13, 33
7	2.8	3488.42	6, 7, 12, 14, 15	115	17, 25, 25, 14, 34
8	3.1	3497.41	6, 7, 12, 14, 15	120	18, 27, 26, 15, 34
9	3.4	3508.09	6, 7, 12, 14, 15	124	19, 29, 27, 15, 34
10	3.7	3520.09	6, 7, 12, 14, 15	129	20, 31, 28, 16, 34
11	4.0	3532.19	6, 7, 12, 14, 15	134	21, 33, 29, 17, 34
12	4.3	3543.86	6, 7, 12, 14, 15	140	22, 36, 30, 18, 34

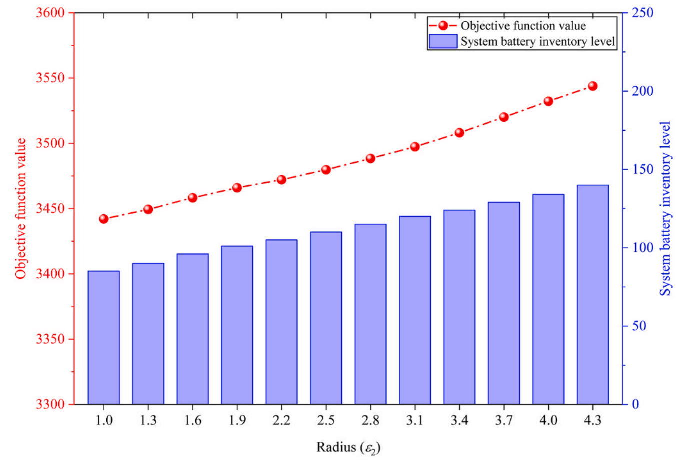

Fig. 5. Objective value and system battery inventory level under different radii.

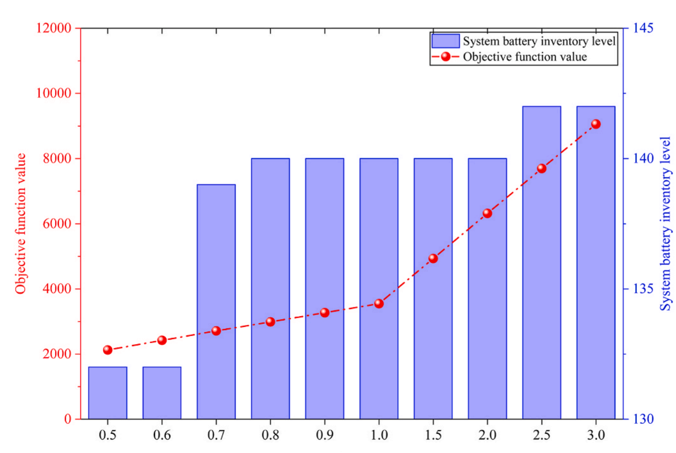

Fig. 6. Objective value and system battery inventory level under different transportation costs.

Table 5
Optimal solutions obtained under different unit transportation costs.

No.	Cost (β)	Objective function value	Location of BSS	System battery inventory level	Battery inventory levels at each BSS
1	50%	2125.22	6, 7, 13, 15	132	30, 35, 33, 34
2	60%	2421.19	6, 7, 13, 15	132	30, 35, 33, 34
3	70%	2710.38	6, 7, 12, 14, 15	139	22, 35, 30, 18, 34
4	80%	2988.33	6, 7, 12, 14, 15	140	22, 36, 30, 18, 34
5	90%	3266.09	6, 7, 12, 14, 15	140	22, 36, 30, 18, 34
6	100%	3543.85	6, 7, 12, 14, 15	140	22, 36, 30, 18, 34
7	150%	4932.68	6, 7, 12, 14, 15	140	22, 36, 30, 18, 34
8	200%	6318.73	6, 7, 12, 14, 15	140	22, 36, 30, 18, 34
9	250%	7695.06	6, 7, 12, 13, 14, 15	142	22, 35, 30, 6, 15, 34
10	300%	9058.40	6, 7, 12, 13, 14, 15	142	22, 35, 30, 6, 15, 34

relatively stable response compared with the topological changes in the network. The total system battery inventory only marginally increases, moving from 132 units in the lowest-cost scenario to 142 units in the highest-cost scenario. This suggests that the model primarily mitigates the risk of high transportation costs through spatial optimization—altering where the stations are located—rather than by significantly manipulating the inventory depth at each station. The slight increase in total inventory in the higher-cost scenarios is largely a byproduct of opening additional facilities, which inherently requires a baseline level of stock to remain operational.

6.3.3. *Sensitivity analysis of the inventory limits of BSSs*

In this subsection, the sensitivity of the model's optimal solution to variations in the maximum inventory capacity of the BSS is examined. The parameter $\bar{y}_j$, which represents the inventory limit of node $j \in \mathscr{D}$, is varied from 55% to 110% of the baseline capacity to simulate scenarios ranging from strict resource constraints to ample battery storage availability. As illustrated in Table 6 and Fig. 7, the objective function value clearly monotonically decreases as the inventory limit decreases, from 3969.53 at the 55% level to 3531.40 at the 110% level. This downward trend indicates that tighter capacity constraints impose significant penalties on the transportation system, likely because the model is forced to adopt suboptimal routing or facility configurations to satisfy demand. As the capacity constraints are relaxed, the system gains the flexibility to store more batteries at optimal locations, thereby reducing total generalized costs. Notably, the rate of cost reduction diminishes as the percentage increases, suggesting that beyond a certain threshold (approximately 100%), the marginal benefit of adding further capacity decreases.

The impact of capacity constraints is most visibly reflected in strategic decisions regarding BSS location. At the most constrained level (55% and 60%), the model is forced to open a larger network of facilities, selecting 7 nodes (i.e., nodes 6, 7, 8, 12, 13, 14, and 15) to distribute the battery inventory. This suggests that when individual station capacity is insufficient to handle local demand surges, the transportation system must compensate by expanding infrastructure to spread the inventory burden. However, as the capacity limit decreases to 80% and above, a consolidation effect is observed; the optimal number of BSSs decreases to 5 stable nodes (i.e., nodes 6, 7, 12, 14, and 15). Specifically, nodes such as nodes 8 and 13 are phased out of the solution set. This demonstrates that with sufficient capacity, the model prefers a more centralized network configuration, utilizing fewer, higher-capacity hubs rather than a dispersed network of smaller stations.

Table 6
Optimal solutions obtained under different inventory limits.

No.	$\bar{y}_j$	Objective function value	Location of BSS	System battery inventory level	Battery inventory levels at each BSS
1	55%	3969.53	6, 7, 8, 12, 13, 14, 15	134	23, 23, 17, 17, 19, 17, 18
2	60%	3854.20	6, 7, 8, 12, 13, 14, 15	141	23, 25, 18, 19, 21, 15, 20
3	65%	3803.76	6, 7, 12, 13, 14, 15	135	27, 27, 20, 22, 17, 22
4	70%	3754.34	6, 7, 12, 13, 14, 15	137	27, 29, 22, 21, 15, 23
5	75%	3685.75	6, 7, 12, 13, 15	133	27, 31, 24, 26, 25
6	80%	3622.46	6, 7, 12, 14, 15	135	22, 33, 25, 28, 27
7	85%	3609.59	6, 7, 12, 14, 15	137	22, 35, 27, 25, 28
8	90%	3587.01	6, 7, 12, 14, 15	136	23, 37, 28, 18, 30
9	95%	3552.59	6, 7, 12, 14, 15	139	22, 37, 30, 18, 32
10	100%	3543.86	6, 7, 12, 14, 15	140	22, 36, 30, 18, 34
11	105%	3539.62	6, 7, 12, 14, 15	140	22, 35, 30, 18, 35
12	110%	3531.40	6, 7, 12, 14, 15	140	22, 33, 30, 18, 37

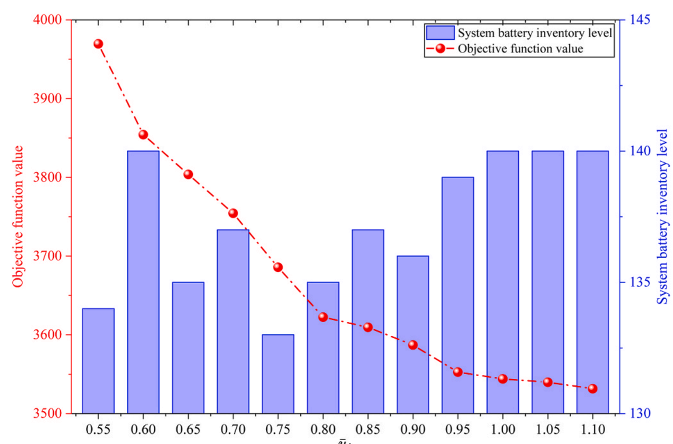

Fig. 7. Objective value and system battery inventory level under different inventory limits.

Furthermore, the distribution of the battery inventory across the selected nodes provides insight into this consolidation phenomenon. While the total system inventory remains relatively stable—fluctuating slightly between 133 and 141 units—the allocation at individual nodes changes drastically. Under tight constraints (e.g., 55%), the inventory is evenly distributed, with most stations holding between 17 and 23 units and hovering near their caps. Conversely, in the unconstrained scenarios (e.g., 110%), the inventory variance increases significantly. Key nodes, particularly nodes 7 and 15, absorb much higher inventory loads (33 and 37 units, respectively), effectively acting as primary reservoirs for the network. This analysis confirms that increasing the physical capacity of BSSs allows for a more efficient, consolidated inventory management strategy, reducing the need for redundant facility construction.

6.3.4. *Sensitivity analysis of the expected necessary battery swapping demand*

In this subsection, the sensitivity of the optimization results to variations in the expected necessary battery swapping demand, denoted by the mean vector $\boldsymbol{u}$, is investigated. This parameter is critical for understanding transportation system scalability in the face of increasing CEV adoption rates or seasonal fluctuations. In the experimental design, the baseline expected demand $\boldsymbol{u}$ is multiplied by a scaling factor ranging from 90% to 200%. As presented in Table 7 and Fig. 8, the objective function value steadily and monotonically increases as $\boldsymbol{u}$ increases, from 3522.87 in the 90% scenario to 3885.14 in the 200% scenario. Concurrently, the total system battery inventory exhibits a growth trajectory, expanding from 133 units to 204 units. This direct correlation confirms that the primary mechanism for absorbing increased mean demand is the proportional acquisition of battery assets, ensuring that service levels are maintained.

A deeper analysis of BSS location decisions reveals the dynamic evolution of the network topology driven by demand. In the lower demand regimes (i.e., 90% to 120%), the optimal configuration remains stable with a five-node set (i.e., nodes 6, 7, 12, 14, and 15). However, as demand surpasses the 130% threshold, a distinct topological reconfiguration occurs: Node 14 is replaced by Node 13. This substitution suggests that as the traffic volume intensifies, Node 13 offers a superior distinct advantage—likely due to better centrality or capacity potential—rendering it a more strategic location for heavy-load scenarios than Node 14 does. As demand pressure continues to increase to extreme levels (180% and above), the transportation system undergoes spatial expansion. The network reverts to include Node 14 alongside the existing set, resulting in a six-node configuration (i.e., nodes 6, 7, 12, 13, 14, and 15). This shift indicates that at very high demand levels, spatial substitution is no longer sufficient; the system must physically expand its footprint to disperse the battery swapping load.

The inventory allocation at individual nodes further elucidates the constraints driving these topological shifts. It is observable that certain nodes, such as Node 7, reach a saturation point early in the progression; its inventory stabilizes at 42 units once demand hits 140% and does not increase further, implying that it has hit a capacity or utility ceiling. Consequently, the burden of the additional demand in the highest scenarios (190%–200%) is disproportionately shifted to other facilities, most notably Node 6, where inventory levels surge from approximately 24 units to 43 units. This localized saturation explains the necessity for the network expansion observed in the final rows of the table; when prime locations such as Node 7 are maximized, the model is mathematically forced to open valid secondary locations (re-introducing Node 14) to accommodate the excess necessary battery inventory.

Table 7
Optimal solutions obtained under different expected demands.

No.	$\boldsymbol{u}$	Objective function value	Location of BSS	System battery inventory level	Battery inventory levels at each BSS
1	90%	3522.87	6, 7, 12, 14, 15	133	21, 32, 29, 17, 34
2	100%	3543.86	6, 7, 12, 14, 15	140	22, 36, 30, 18, 34
3	110%	3561.17	6, 7, 12, 14, 15	145	22, 39, 32, 18, 34
4	120%	3591.35	6, 7, 12, 14, 15	151	24, 42, 32, 19, 34
5	130%	3634.23	6, 7, 12, 13, 15	157	24, 42, 32, 25, 34
6	140%	3655.16	6, 7, 12, 13, 15	163	24, 42, 32, 31, 34
7	150%	3675.28	6, 7, 12, 13, 15	167	24, 42, 32, 35, 34
8	160%	3729.25	6, 7, 12, 13, 15	175	32, 42, 32, 35, 34
9	170%	3773.15	6, 7, 12, 13, 15	182	39, 42, 32, 35, 34
10	180%	3820.30	6, 7, 12, 13, 14, 15	191	34, 42, 32, 32, 17, 34
11	190%	3852.52	6, 7, 12, 13, 14, 15	198	38, 42, 32, 34, 18, 34
12	200%	3885.14	6, 7, 12, 13, 14, 15	204	43, 42, 32, 35, 18, 34

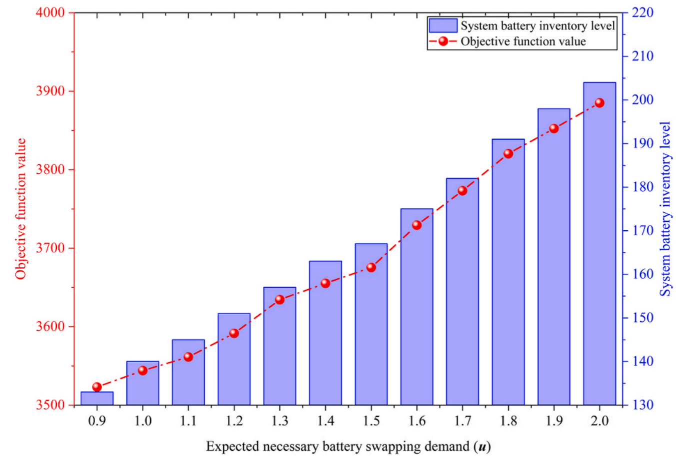

Fig. 8. Objective value and system battery inventory level under different expected demands.

6.3.5. *Sensitivity analysis of the BSS construction cost*

To comprehensively evaluate the robustness of our infrastructure investment assumptions and investigate the model's adaptability to varying capital expenditures, we conduct a sensitivity analysis on the BSS daily construction cost (c_j). We scale the baseline construction cost from 20% to 200%, and the corresponding optimal deployment strategies and system costs are summarized in Table 8.

A monotonic increase in the objective function value is observed, rising from 3420.48 to 4815.76 as capital expenditure increases. More importantly, the optimal network topology exhibits a highly logical spatial consolidation trend in response to rising infrastructure costs. When the construction cost is relatively low (20–40% of the baseline), the model adopts a decentralized strategy by constructing 6 BSSs (locations 6, 7, 12, 13, 14, and 15). This widespread deployment minimizes the routing distances and operational costs for the fleets. However, as capital investment becomes increasingly prohibitive, the model strategically eliminates marginal BSS locations to control fixed costs. The network consolidates to 5 core stations at the baseline level (60%–140%) and further shrinks to a highly centralized configuration of only 4 stations (locations 6, 7, 13, and 15) when the cost reaches 160%–200%. Concurrently, the battery inventory allocation clearly demonstrates a risk-pooling effect. Although the total number of deployed BSSs

Table 8
Optimal solutions obtained under different construction cost levels.

No.	c_j	Objective function value	Location of BSS	System battery inventory level	Battery inventory levels at each BSS
1	20%	3420.48	6, 7, 12, 13, 14, 15	141	22, 35, 30, 6, 14, 34
2	40%	3551.28	6, 7, 12, 13, 14, 15	141	22, 35, 30, 6, 14, 34
3	60%	3664.94	6, 7, 12, 14, 15	140	22, 36, 30, 18, 34
4	80%	3773.94	6, 7, 12, 14, 15	140	22, 36, 30, 18, 34
5	100%	3882.94	6, 7, 12, 14, 15	140	22, 36, 30, 18, 34
6	120%	3991.94	6, 7, 12, 14, 15	140	22, 36, 30, 18, 34
7	140%	4100.94	6, 7, 12, 14, 15	140	22, 36, 30, 18, 34
8	160%	4205.36	6, 7, 13, 15	132	30, 35, 33, 34
9	180%	4292.56	6, 7, 13, 15	132	30, 35, 33, 34
10	200%	4815.76	6, 7, 13, 15	132	30, 35, 33, 34

decreases from 6 to 4, the system battery inventory level decreases only marginally from 141 to 132. Instead of a proportional reduction, the model densifies the inventory buffers at the surviving central hubs to maintain the stringent 95% service level mandated by the joint chance constraints. For instance, as the network shrinks to 4 stations, the inventory at BSS 6 increases from 22 to 30 units to absorb the rerouted charging demand. These results rigorously confirm that the proposed DRO framework optimally and dynamically balances fixed facility capital expenditures against variable EV routing and inventory holding costs across diverse real-world economic scenarios.

6.3.6. Sensitivity analysis of the confidence level of the joint chance constraint

In risk-aware planning for transportation systems, the confidence level of the risk metric represents the degree of conservatism of the decision maker. To quantify its impact on our DRO framework, we conduct a sensitivity analysis on the confidence level of the joint chance constraint (denoted as α'). According to the analytical reformulation established in Proposition 4, α' is mathematically controlled by the robustness parameter ε_2 via the exact relationship $\varepsilon_2 = \sqrt{\alpha'/(1-\alpha')}$. Therefore, we simulate different risk appetites by varying α' from 0.80 ($\varepsilon_2 = 2$) to an extreme risk-averse level of 0.99 ($\varepsilon_2 = 9.95$). The detailed results are summarized in Table 9.

As illustrated in Table 9, both the total expected cost and the optimal system battery inventory level are highly sensitive to the chosen confidence level. When α' is relatively low (e.g., 0.80), the decision maker tends to be moderately conservative, resulting in a lower baseline inventory requirement (102 units) and minimized total costs (3807.36). Within the moderate to high confidence range ($\alpha' \in [0.80, 0.96]$), the topological configuration of the BSS network remains remarkably stable, and 5 nodes (locations 6, 7, 12, 14, and 15) are consistently selected. The model mitigates the increasing risk primarily by densifying the inventory buffer at these existing stations rather than expanding the infrastructure. However, an intriguing structural shift occurs as the confidence level approaches the extreme tail-risk spectrum ($\alpha' \geq 0.98$). At $\alpha' = 0.99$, the model heavily penalizes extremely rare but severe demand surges. To robustly satisfy this stringent 99% reliability requirement, the system must drastically expand its inventory buffer to 218 units. Because the existing 5-node configuration reaches its physical capacity limits (e.g., node 7 stabilizes at 42 units), the system is mathematically forced to undergo spatial expansion, opening an additional facility (Node 13) to accommodate the massive required inventory. This infrastructural expansion, combined with massive inventory holding costs, precipitates a steep, non-linear surge in the total expected cost to 4340.22. This explicit trade-off directly quantifies the "price of conservatism" inherent in stochastic optimization. It provides actionable insights for decision makers, highlighting that hedging against extreme black swan disruptions requires not only deeper inventory buffers but also, ultimately, costly physical network expansion.

Table 9
Optimal solutions obtained under different confidence levels.

No.	α'	Objective function value	Location of BSS	System battery inventory level	Battery inventory levels at each BSS
1	0.80	3807.36	6, 7, 12, 14, 15	102	14, 22, 23, 12, 31
2	0.85	3816.97	6, 7, 12, 14, 15	108	15, 24, 24, 13, 32
3	0.90	3832.19	6, 7, 12, 14, 15	118	17, 27, 26, 14, 34
4	0.92	3846.59	6, 7, 12, 14, 15	124	19, 29, 27, 15, 34
5	0.94	3869.34	6, 7, 12, 14, 15	134	21, 33, 29, 17, 34
6	0.96	3904.31	6, 7, 12, 14, 15	149	24, 40, 32, 19, 34
7	0.98	4048.29	6, 7, 12, 13, 15	176	33, 42, 32, 35, 34
8	0.99	4340.22	6, 7, 12, 13, 14, 15	218	43, 42, 32, 35, 32, 34

6.4. Out-of-sample test

To rigorously evaluate the generalizability and reliability of the optimal solutions derived from the proposed DRO model, we conduct a comprehensive out-of-sample analysis via Monte Carlo simulation. Since the true probability distribution of swapping demand in real-world applications is often unknown and may deviate from the worst-case distribution identified by the DRO framework, verifying whether the constructed transportation system can sustain service levels under various potential ground truth scenarios is crucial. To quantify the system's reliability, we introduce two key probabilistic metrics: the average individual probability (AIP) and the average joint probability (AJP). The AIP measures the likelihood that a single BSS satisfies its local necessary battery swapping demand constraints, averaged across all the BSSs and simulation scenarios, thereby reflecting the component-level reliability. In contrast, the AJP imposes a stricter criterion, measuring the probability that the entire transportation system satisfies all necessary battery swapping demand constraints simultaneously within a given scenario, thus serving as an indicator of system-wide resilience. The calculation methods are shown in Equations (61) and (62):

$$AIP = \frac{1}{N|\mathscr{D}|}\sum_{n\in[N]}\sum_{j\in\mathscr{D}}\mathbb{I}\left(\sum_{i\in\mathscr{O}}\widehat{\zeta}_i^n z_{ij} \leq y_j\right) \tag{61}$$

$$AJP = \frac{1}{N}\sum_{n\in[N]}\mathbb{I}\left(\sum_{i\in\mathscr{O}}\widehat{\zeta}_i^n z_{ij} \leq y_j, \forall j\in\mathscr{D}\right). \tag{62}$$

In the simulation experiments, we generate random demand samples from three distinct probability distributions to emulate diverse uncertainty patterns with a parameter k: the truncated uniform distribution (TUN) $\zeta_i \sim \mathbb{U}(u_i - k\sqrt{3}\tau_i, \mu_i + k\sqrt{3}\tau_i)$, the truncated normal distribution (TNO) $\zeta_i \sim \mathbb{N}\left(u_i, (k\tau_i)^2\right)$, and the log-normal distribution (LN) $\zeta_i \sim \mathbb{L}\left(u_i^{\mathrm{L}}, (k\tau_i^{\mathrm{L}})^2\right)$, where $u_i^L = \ln\left((u_i)^2/\sqrt{(u_i)^2 + (\tau_i)^2}\right)$ and $\tau_o^{\mathrm{L}} = \ln(1 + (u_i)^2/(\tau_i)^2)$. These distributions are selected to capture different statistical characteristics of demand fluctuations. The TUN represents scenarios with bounded uncertainty where demand is evenly distributed within a specific interval; the TNO approximates the standard symmetric deviations often observed in traffic flows, with truncation ensuring non-negative values; and the LN is utilized to model asymmetric, heavy-tailed demand patterns that frequently occur in logistics systems. By testing the model against these varied distributional forms, we can assess the robustness of the optimal BSS configuration against distributional misspecification. The parameter settings for these distributions are grounded in the first two moments (mean $\boldsymbol{u}$ and standard deviation τ_i) of the baseline dataset (see Table 1). To further investigate the sensitivity of the solution to the magnitude of uncertainty, we introduce a scaling parameter k that modulates the dispersion of the generated demand. Specifically, for the TUN, k controls the width of the support interval; for the TNO and LN, it scales with the standard deviation of the underlying distribution. In our analysis, we fix the sample size N at 10,000 for each scenario to ensure statistical significance. By varying k, we systematically expand the range of demand fluctuations, allowing us to observe how the reliability metrics (i.e., AIP and AJP) evolve as the environment becomes increasingly volatile, thereby validating the price of robustness paid by the DRO model.

The numerical results presented in Fig. 9 and Table 10 provide compelling evidence of the robustness of the proposed DRO against distributional mismatches. With respect to the degree of low-to-

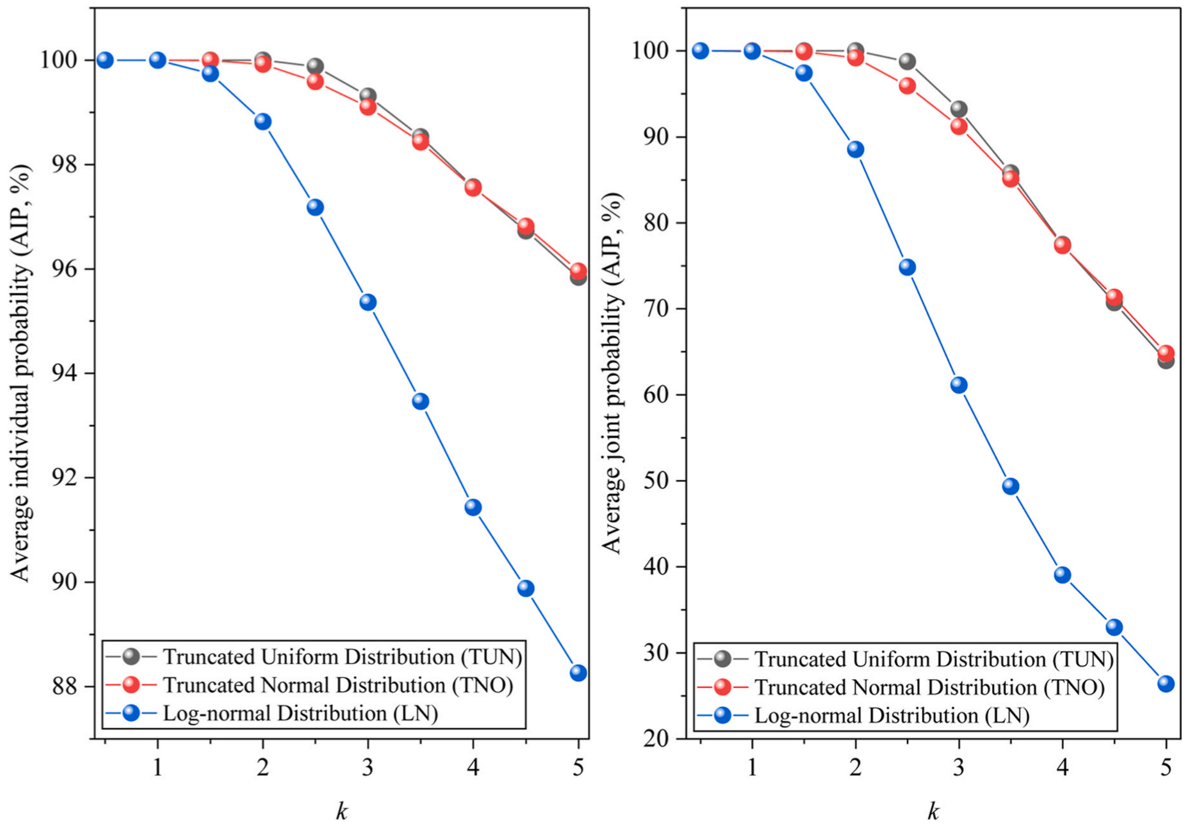

Fig. 9. AIP and AJP under different k values.

Table 10
AIP and AJP with different values of k.

No.	k	AIP (%)			AJP (%)		
		TUN	TNO	LN	TUN	TNO	LN
1	0.5	100.00	100.00	100.00	100.00	100.00	100.00
2	1.0	100.00	100.00	100.00	100.00	100.00	99.95
3	1.5	100.00	99.99	99.74	100.00	99.90	97.42
4	2.0	100.00	99.92	98.82	100.00	99.20	88.55
5	2.5	99.88	99.59	97.18	98.76	95.93	74.84
6	3.0	99.31	99.10	95.36	93.22	91.21	61.13
7	3.5	98.53	98.43	93.46	85.80	85.11	49.35
8	4.0	97.57	97.55	91.43	77.48	77.35	39.03
9	4.5	96.73	96.82	89.88	70.71	71.35	32.96
10	5.0	95.84	95.96	88.26	63.96	64.80	26.37

moderate uncertainty, specifically when the scaling parameter k ranges from 0.5 to 1.5, the model demonstrates exceptional reliability. Across all three tested distributions—TUN, TNO, and LN—the AIP maintains a near-perfect level of 100%, and the AJP remains above 97%. These findings indicate that when the actual demand fluctuations are within a reasonable range of the estimated parameters, the optimal solution derived from the DRO model is capable of fully satisfying system demand without incurring capacity violations. This stability confirms that the ambiguity set constructed in the model effectively covers the true probability distributions when the variance is comparable to the baseline estimation.

As the uncertainty scaling parameter k increases beyond 2.0, representing increasingly volatile and extreme demand scenarios, a distinct divergence between the component-level metric (i.e., AIP) and the system-level metric (i.e., AJP) emerges. The AIP exhibits remarkable resilience; even when the demand variance is amplified by a factor of 5.0, the average individual reliability remains high, ranging from 88.26% to 95.84% across all distributions. This suggests that strategic location and capacity planning decisions are sufficiently conservative to protect individual facilities against severe demand surges. However, the response of the AJP to extreme variance is more sensitive. This is theoretically expected, as AJP requires the simultaneous satisfaction of constraints across the entire network; a failure at a single node compromises the metric for the whole system. Nevertheless, for symmetric distributions such as TUN and TNO, the system reliability remains relatively robust, maintaining an AJP of approximately 64–70% even under the most extreme stress test (i.e., when k equals 5.0), which is a commendable performance for a static plan facing five times the standard deviation of demand. It is particularly noteworthy to analyze the performance disparity between the distributions. The model performs most reliably under the TUN and TNO, which share symmetric characteristics. In contrast, the LN distribution poses the most significant challenge to the system, particularly with respect to the AJP metric. As k increases to 5.0, while the AJP for TUN and TNO remains above 60%, the AJP for the LN distribution decreases to 26.37%. This performance gap can be attributed to the heavy-tailed and asymmetric nature of the LN distribution. At high k values, the LN distribution generates extreme positive demand outliers that are far more severe than those in symmetric distributions. These outliers are likely to breach the capacity of specific BSS nodes, triggering a system-level violation. Despite this, the fact that the AIP for the LN distribution remains near 90% even at $k = 5.0$ underscores the effectiveness of the proposed DRO approach: while it may not guarantee 100% system-wide perfection under extreme, heavy-tailed outliers, it successfully prevents widespread network collapse by ensuring that the vast majority of facilities remain operational. The out-of-sample analysis also serves as a stress test for the reliability of our moment-based assumptions. By generating demand samples from asymmetric and heavy-tailed distributions (e.g., log-normal), we evaluate whether the ambiguity set constructed using only the first two moments is sufficient to cover extreme realizations.

7. Model extension

While the proposed DRO framework effectively identifies robust locations for fixed BSSs, the rapid evolution of the EV ecosystem introduces new paradigms for energy replenishment. In recent years, mobile battery swapping vehicles (MBSVs)—specialized trucks equipped with mobile battery storage and swapping mechanisms—have emerged as a flexible alternative to permanent infrastructure. Industry leaders such as NIO and various emergency power support providers have begun deploying mobile units to address temporary demand surges, distinct *tidal* traffic patterns, or emergency rescue scenarios where fixed infrastructure is either unavailable or overwhelmed. In this section, we extend the original CBLIP model to consider MBSVs. To characterize this new transportation system mathematically, we introduce a new set of decision variables and constraints to the first-stage problem. Let w_j denote the number of MBSVs deployed at candidate node $j \in \mathscr{D}$. Unlike the fixed inventory y_j, which incurs a lower unit holding cost h_j but is spatially immobile, the mobile inventory provided by w_j incurs a higher unit operating cost p_j (reflecting driver wages and vehicle depreciation) but serves as an adjustable buffer. The logical modification to the original model is straightforward. The total service capacity at any node $j \in \mathscr{D}$ is now the sum of its fixed inventory and the mobile capacity.

First stage of Model:

$$\min_{(\boldsymbol{x},\boldsymbol{y},\boldsymbol{w})} \sum_{j\in\mathscr{D}} \left(c_j x_j + h_j y_j + p_j w_j\right) + \sup_{F\in\mathscr{F},G\in\mathscr{G}} \mathbb{E}_{F,G}[g(\boldsymbol{n},\boldsymbol{\xi},\boldsymbol{\zeta})] \tag{63}$$

$$s.t.\ y_j \le \overline{y}_j x_j\ \forall j \in \mathscr{D} \tag{64}$$

$$w_j \le \overline{w}_j\ \forall j \in \mathscr{D} \tag{65}$$

$$\boldsymbol{x} \in \{0,1\}^{|\mathscr{D}|} \tag{66}$$

$$\boldsymbol{y} \in \mathbb{Z}_+^{|\mathscr{D}|} \tag{67}$$

$$\boldsymbol{w} \in \mathbb{Z}_+^{|\mathscr{D}|} \tag{68}$$

where $\boldsymbol{w} = (w_j)$ represents an integer decision variable representing the number of MBSVs deployed at node $j \in \mathscr{D}$; $\overline{w}_j$ denotes the maximum allowable number of MBSVs that can be deployed at a single candidate node; and p_j represents the unit (daily) deployment and operational cost of a single MBSV. At this point, the capacity constraint and demand satisfaction logic are updated as follows:

$$\mathbb{P}_G\left(\sum_{i\in\mathscr{O}} \zeta_i z_{ij} \le y_j + C^{\mathrm{M}} w_j, \forall j \in \mathscr{D}\right) \ge 1-\alpha\ \forall G \in \mathscr{G} \tag{69}$$

where C^{M} represents the battery carrying capacity of a single MBSV.

On the basis of the above model, we conduct a comparative analysis between the extended model incorporating MBSVs and the original model. The operational parameters for the MBSVs are calibrated with a unit deployment cost of 70, a battery capacity of 15 units, and a deployment cap of 2 vehicles per node. As detailed in Table 11, the integration of mobile resources yields a tangible reduction in the total cost, decreasing from 4251.81 to 4231.94. While the marginal improvement in the objective value might appear modest, the underlying transformation in the network topology offers profound managerial insights into asset allocation under uncertainty. Specifically, Nodes 6 and 7 emerge as the core backbone of the service network. Regardless of the availability of mobile units, the model consistently selects these locations for permanent BSS construction and allocates high inventory levels (e.g., Node 7 maintains an inventory of more than 40 units in both scenarios). This invariance suggests that for geographically central locations with high demand density, fixed infrastructure remains the most economically viable solution.

Moreover, in the extended model, some fixed facilities are eliminated and replaced by MBSVs. For example, at Node 15, the previous requirement for a fixed station with 31 batteries is efficiently substituted by 2 MBSVs, providing a comparable flexible capacity of 30 units. This substitution allows the transportation system to avoid high fixed construction costs at locations where the price of robustness is otherwise too steep. Furthermore, the granular scalability of mobile units facilitates network expansion; Node 13, which was previously unselected owing to the prohibitive cost of a full station, is now activated with a single MBSV. These findings confirm that the inclusion of MBSVs mitigates the conservatism inherent in the DRO model. This approach not only lowers the capital barrier for network expansion but also enhances the system's agility, indicating that operational flexibility is a powerful substitute for redundant static infrastructure in highly uncertain environments.

Table 11
Optimal solutions for models considering MBSV and not considering MBSV.

Node	Model with MBSV (Objective value = 4231.94)			Model without MBSV (Objective value = 4251.81)	
	x_j	y_j	w_j	x_j	y_j
6	1	33	0	1	33
7	1	41	0	1	40
12	0	0	2 (30 batteries)	1	20
13	0	0	1 (15 batteries)	0	0
14	0	0	1 (15 batteries)	1	37
15	0	0	2 (30 batteries)	1	31

8. Conclusions

This paper addresses the infrastructure planning problem for CEVs by developing a distributionally robust decision-making framework for the location and inventory management of BSSs. Motivated by the limitations of traditional stochastic and robust optimization, this study makes three primary contributions. First, we develop a two-stage DRO model that jointly optimizes station location, inventory pre-positioning, and demand allocation while explicitly enforcing network-wide service reliability via a joint chance constraint. Second, we derive a tractable reformulation. By employing a CVaR-based approximation, the intractable joint chance-constrained model is rigorously converted into a solvable parametric SOCP. Third, we develop a tailored OAA that exploits the convex conic structure of the reformulated model, ensuring practical implementation ability for large-scale infrastructure planning. The comprehensive numerical experiments yield the following key conclusions.

First, the proposed framework reveals a clear distinction between strategic stability and operational divergence. Unlike the deterministic model, the DRO model often preserves the same core BSS locations while substantially increasing inventory buffers and diversifying demand allocation. This finding indicates that strategic facility locations are relatively stable under demand ambiguity, whereas operational protection is achieved mainly through stronger inventory deployment and more diversified service patterns. In this sense, the price of robustness is paid primarily in inventory rather than in wholesale spatial redesign. The additional investment is economically meaningful: supplementary ex-post analysis shows that although the DRO solution has a higher upfront planning cost, it becomes economically preferable once demand volatility is sufficiently severe because outage penalties under the deterministic solution rise rapidly beyond the crossover threshold.

Second, the proposed OAA is computationally effective. Benchmark tests against DICOPT show that the customized algorithm remains highly tractable as the network size increases. While DICOPT performs comparably only on the smallest instances, its runtime increases sharply, and it fails to solve larger cases within the 3600 s time limit. In contrast, the proposed OAA solves even the largest tested instance in 13.51 s on average, with the iteration count remaining below 27. These results confirm that the tractable reformulation and tailored algorithm together make the framework computationally suitable for strategic network planning.

Third, the sensitivity analyses reveal several robust structural patterns. The results of the ambiguity-radius analysis reveal that higher distributional uncertainty leads mainly to denser inventory buffers, while facility locations remain relatively stable. Transportation cost and inventory capacity analyses reveal a centralization–decentralization trade-off: higher transportation costs favor denser networks, whereas looser capacity limits encourage consolidation. The expected-demand analysis confirms that long-term fleet growth drives mainly higher system costs and greater inventory deployment. In addition, rising construction costs induce network consolidation, whereas stricter reliability requirements initially increase inventories at existing stations and, at very high confidence levels, may eventually trigger additional facility deployment. Together, these findings suggest that the spatial network is structurally resilient over a wide parameter range, while inventory acts as the primary buffer against economic and uncertainty-driven stress.

Fourth, the out-of-sample analyses confirm the practical value of the DRO framework. Under multiple demand distributions, including the truncated uniform, truncated normal, and log-normal cases, the model maintains strong reliability performance, with near-perfect system-wide reliability in moderate-variance regimes and robust component-level reliability even under severe heavy-tailed demand. Moreover, the comparison with stochastic programming and robust optimization shows that the DRO model provides a more balanced trade-off between economy and protection: it avoids the under-protection of the SP solution and the excessive conservatism of the RO solution while sustaining high service reliability under distributional uncertainty.

Fifth, the extension to a fixed-mobile hybrid battery swapping system highlights the value of operational flexibility. Mobile battery swapping vehicles can replace fixed stations at peripheral or highly volatile locations while preserving fixed facilities at core demand hubs. This reduces excessive static investment and suggests that flexible mobile resources can mitigate the conservatism of purely fixed infrastructure planning.

Future research can extend this paper by incorporating multi-period dynamic planning to address the temporal evolution of EV adoption. Specifically, extending our strategic framework into a fixed-mobile hybrid battery swapping system would be highly promising. To fully realize this hybrid concept, future studies must explicitly address the operational constraints of mobile swapping vehicles (e.g., limited onboard capacity and service time windows), investigate dynamic routing and scheduling decisions within a stochastic traffic network, and resolve the mathematical challenges of their integration with the strategic-level optimization model. Additionally, integrating heterogeneous battery specifications and vehicle-to-grid technologies would provide a more holistic perspective on the energy ecosystem.

CRediT authorship contribution statement

Xu Xin: Writing – review & editing, Writing – original draft, Visualization, Validation, Software, Methodology, Investigation, Formal analysis, Data curation, Conceptualization. **Tao Zhang:** Writing – review & editing, Writing – original draft, Visualization, Validation, Supervision, Software, Methodology, Investigation, Formal analysis, Conceptualization. **King-Wah Pang:** Writing – review & editing, Writing – original draft, Validation, Supervision, Methodology, Investigation, Funding acquisition, Formal analysis, Conceptualization. **Jun Zhao:** Writing – review & editing, Writing – original draft, Validation, Resources, Investigation, Formal analysis. **Shuaian Wang:** Writing – review & editing, Writing – original draft, Validation, Software, Resources, Methodology, Investigation.

Declaration of competing interest

The authors declare that they have no known competing financial interests or personal relationships that could have appeared to influence the work reported in this paper.

Acknowledgments

This work was supported by the National Natural Science Foundation of China [Grant No. 72371221] and the Research Grants Council of the Hong Kong Special Administrative Region, China [Project number HKSAR RGC TRS T32-707/22-N].

Appendix A. Supplementary data

Supplementary data to this article can be found online at https://doi.org/10.1016/j.energy.2026.141090.

Data availability

Data will be made available on request.

References

[1] Cheng K, Zou Y, Xin X, Gong S. Optimal Lane expansion model for a battery electric vehicle transportation network considering range anxiety and demand uncertainty. J Clean Prod 2020;276:124198.
[2] Alberizzi JC, Callioni F, Estévez MAP, Renzi M. Optimized integration of charging and battery swapping stations for peak load and cost reduction. Energy 2026: 139683.
[3] Guo Y, Yan K, Qian X, Li X, Hu Y, Wang N. A robust optimal battery swapping station location model for commercial electric vehicles under demand uncertainty. Energy 2025:137466.
[4] Peng T, Ren L, Ou X. Development and application of life-cycle energy consumption and carbon footprint analysis model for passenger vehicles in China. Energy 2023;282:128412.
[5] Dudek E. The flexibility of domestic electric vehicle charging: the electric nation project. IEEE Power Energy Mag 2021;19(4):16–27.
[6] Ren L, Zhou S, Peng T, Ou X. Greenhouse gas life cycle analysis of China's fuel cell medium-and heavy-duty trucks under segmented usage scenarios and vehicle types. Energy 2022;249:123628.
[7] Zhang S, Chen M, Zhang W. A novel location-routing problem in electric vehicle transportation with stochastic demands. J Clean Prod 2019;221:567–81.
[8] Hadley SW, Tsvetkova AA. Potential impacts of plug-in hybrid electric vehicles on regional power generation. Electr J 2009;22(10):56–68.
[9] Feng J, Hou S, Yu L, Dimov N, Zheng P, Wang C. Optimization of photovoltaic battery swapping station based on weather/traffic forecasts and speed variable charging. Appl Energy 2020;264:114708.
[10] Ali MI, Mandal RK, Kumar A. Optimization of battery swapping station for electric vehicles by novel adaptive GWO algorithm. Energy 2025;333:137348.
[11] Xin X, Zhang T, Li C, Liu Y, Gao L, Du Y. A battery electric vehicle transportation network design model with bounded rational travelers. J Adv Transp 2023;2023 (1):6506169.
[12] Li B, Szeto W, Zou L. Optimal fare and fleet size regulation in a taxi/ride-sourcing market with congestion effects, emission externalities, and gasoline/electric vehicles. Transport Res Pol Pract 2022;157:215–43.
[13] Morro-Mello I, Padilha-Feltrin A, Melo JD, Calviño A. Fast charging stations placement methodology for electric taxis in urban zones. Energy 2019;188: 116032.
[14] Lai Z, Li S. Towards a multimodal charging network: joint planning of charging stations and battery swapping stations for electrified ride-hailing fleets. Transp Res Part B Methodol 2024;183:102928.
[15] Zentani A, Almaktoof A, Kahn MT. A comprehensive review of developments in electric vehicles fast charging technology. Appl Sci 2024;14(11):4728.
[16] Syla A, Parra D, Patel MK. Assessing flexibility from electric vehicles using an open-source energy system model: trade-offs between smart charging, vehicle-to-grid and an extensive charging infrastructure. Energy 2025:136236.
[17] Clairand J-M, González-Rodríguez M, Kumar R, Vyas S, Escrivá-Escrivá G. Optimal siting and sizing of electric taxi charging stations considering transportation and power system requirements. Energy 2022;256:124572.
[18] Ahmad F, Saad Alam M, Saad Alsaidan I, Shariff SM. Battery swapping station for electric vehicles: opportunities and challenges. IET Smart Grid 2020;3(3):280–6.
[19] Zhang T-y, Yao E-j, Yang Y, Pan L, Li C-p, Li B, et al. Deployment optimization of battery swapping stations accounting for taxis' dynamic energy demand. Transport Res Transport Environ 2023;116:103617.
[20] Cui D, Wang Z, Liu P, Wang S, Dorrell DG, Li X, et al. Operation optimization approaches of electric vehicle battery swapping and charging station: a literature review. Energy 2023;263:126095.

[21] Wu H. A survey of battery swapping stations for electric vehicles: operation modes and decision scenarios. IEEE Trans Intell Transport Syst 2021;23(8):10163–85.
[22] Liang Y, Cai H, Zou G. Configuration and system operation for battery swapping stations in Beijing. Energy 2021;214:118883.
[23] Zhang N, Zhang Y, Ran L, Liu P, Guo Y. Robust location and sizing of electric vehicle battery swapping stations considering users' choice behaviors. J Energy Storage 2022;55:105561.
[24] Wang Z, Hou S. Optimal participation of battery swapping stations in frequency regulation market considering uncertainty. Energy 2024;302:131815.
[25] Infante W, Ma J, Han X, Liebman A. Optimal recourse strategy for battery swapping stations considering electric vehicle uncertainty. IEEE Trans Intell Transport Syst 2019;21(4):1369–79.
[26] An K, Jing W, Kim I. Battery-swapping facility planning for electric buses with local charging systems. Int J Sustain Transp 2020;14(7):489–502.
[27] Sun H, Yang J, Yang C. A robust optimization approach to multi-interval location-inventory and recharging planning for electric vehicles. Omega 2019;86:59–75.
[28] Sarker MR, Pandžić H, Ortega-Vazquez MA. Optimal operation and services scheduling for an electric vehicle battery swapping station. IEEE Trans Power Syst 2014;30(2):901–10.
[29] Wang Z, Hou S, Guo W. Inventory management of battery swapping and charging stations considering uncertainty. Int J Electr Power Energy Syst 2024;155:109528.
[30] Zhang T, Wang S, Xin X. Liner fleet deployment and slot allocation problem: a distributionally robust optimization model with joint chance constraints. Transp Res Part B Methodol 2025;197:103236.
[31] Beraldi P, Bruni ME. A probabilistic model applied to emergency service vehicle location. Eur J Oper Res 2009;196(1):323–31.
[32] Xin X, Zhang T, Wang X, He F, Wu L. Risk-averse distributionally robust optimization for construction waste reverse logistics with a joint chance constraint. Comput Oper Res 2025;173:106829.
[33] Zhang T, Wang S, Xin X. Humanitarian relief logistics network design considering facility location, inventory pre-positioning and evacuation planning: a two-stage distributionally robust optimization approach. Comput Oper Res 2026;189:107390.
[34] Xin X, Wang S, Zhang T. Truck-drone supported humanitarian relief logistics network design: a two-stage distributionally robust optimization approach. Transport Res C Emerg Technol 2025;178:105231.
[35] Kchaou-Boujelben M. Charging station location problem: a comprehensive review on models and solution approaches. Transport Res C Emerg Technol 2021;132:103376.
[36] Shen ZJM, Feng B, Mao C, Ran L. Optimization models for electric vehicle service operations: a literature review. Transp Res Part B Methodol 2019;128:462–77.
[37] Mallahi S, Olamaei J, Fini AS, Montazer BH. A hybrid intelligent decision-making framework for optimal location of electric vehicle battery swapping stations: with an emphasis on sustainable development components. Sustain Cities Soc 2025:106946.
[38] Türk S, Deveci M, Özcan E, Canıtez F, John R. Interval type-2 fuzzy sets improved by simulated Annealing for locating the electric charging stations. Inf Sci 2021;547:641–66.
[39] Li C, Dong Z, Chen G, Zhou B, Zhang J, Yu X. Data-driven planning of electric vehicle charging infrastructure: a case study of Sydney, Australia. IEEE Trans Smart Grid 2021;12(4):3289–304.
[40] Raad NG, Swain C, Ayantayo A, Yang B, Rajendran S. Hybrid regret-based p-robust and distributionally robust optimization models for electric vehicle charging station network design. Comput Ind Eng 2024;198:110709.
[41] Hof J, Schneider M, Goeke D. Solving the battery swap station location-routing problem with capacitated electric vehicles using an AVNS algorithm for vehicle-routing problems with intermediate stops. Transp Res Part B Methodol 2017;97:102–12.
[42] Lin M-D, Liu P-Y, Kuo J-H, Lin Y-H. A multiobjective stochastic location-allocation model for scooter battery swapping stations. Sustain Energy Technol Assessments 2022;52:102079.
[43] Zhou Y, Ong GP, Meng Q, Cui H. Electric bus charging facility planning with uncertainties: model formulation and algorithm design. Transport Res C Emerg Technol 2023;150:104108.
[44] Esmaeilnejad S, Kattan L, Wirasinghe S. Optimal charging station locations and durations for a transit route with battery-electric buses: a two-stage stochastic programming approach with consideration of weather conditions. Transport Res C Emerg Technol 2023;156:104327.
[45] Cheng C, Adulyasak Y, Rousseau L-M. Robust facility location under disruptions. INFORMS Journal on Optimization 2021;3(3):298–314.
[46] Liu Z, Song Z. Robust planning of dynamic wireless charging infrastructure for battery electric buses. Transport Res C Emerg Technol 2017;83:77–103.
[47] Alwesabi Y, Avishan F, Yanıkoğlu İ, Liu Z, Wang Y. Robust strategic planning of dynamic wireless charging infrastructure for electric buses. Appl Energy 2022;307:118243.
[48] Li Y, Shu J, Wang C, Wu T, Wu Y. Robust planning for electric vehicle charging stations under congestion. Transp Res Part B Methodol 2025;200:103291.
[49] He F, Yin Y, Zhou J. Deploying public charging stations for electric vehicles on urban road networks. Transport Res C Emerg Technol 2015;60:227–40.
[50] He J, Yang H, Tang T-Q, Huang H-J. An optimal charging station location model with the consideration of electric vehicle's driving range. Transport Res C Emerg Technol 2018;86:641–54.
[51] Jirdehi MA, Tabar VS. Multi-objective long-term expansion planning of electric vehicle infrastructures integrated with wind and solar units under the uncertain environment considering demand side management: a real test case. Sustain Cities Soc 2023;96:104632.
[52] Jirdehi MA, Shaterabadi M, Tabar VS, Galvani S. Strategic optimization of electric vehicles' battery swapping stations for developing countries: balancing demand, cost dynamics, and sustainability in electric mobility. Energy Sustain Dev 2025;88:101821.
[53] Tabar VS, Tohidi S, Ghassemzadeh S. Risk-constrained day-ahead planning of an energy hub integrated with the on-site hydrogen fueling station and active battery swapping infrastructure considering high level of renewable energies and load redistribution. J Energy Storage 2023;72:108700.
[54] Shaillan HM, Tohidi S, Hagh MT, Tabar VS. Risk-aware two-stage stochastic short-term planning of a hybrid multi-microgrid integrated with an all-in-one vehicle station and end-user cooperation. J Energy Storage 2024;78:110083.
[55] Zhao X, Yang Y, Qin M, Xu Q. Day-ahead dispatch of novel battery charging and swapping station based on distributionally robust optimization. J Energy Storage 2023;63:107080.
[56] Zhou B, Chen G, Huang T, Song Q, Yuan Y. Planning PEV fast-charging stations using data-driven distributionally robust optimization approach based on ϕ-divergence. IEEE Trans Transp Electrif 2020;6(1):170–80.
[57] Guo Y, Yan K, Li X, Qian X, Cheng C. A distributionally robust joint chance constraint optimization model for vehicle battery swapping station location problem. In 2023 China Automation Congress (CAC). IEEE, p. 8575–8580.
[58] Rahmani A, MirHassani S. A hybrid firefly-genetic algorithm for the capacitated facility location problem. Inf Sci 2014;283:70–8.
[59] Chen K, Guo J, Xin X, Zhang T, Zhang W. Port sustainability through integration: a port capacity and profit-sharing joint optimization approach. Ocean Coast Manag 2023;245:106867.
[60] Chauhan D, Unnikrishnan A, Figliozzi M. Maximum coverage capacitated facility location problem with range constrained drones. Transport Res C Emerg Technol 2019;99:1–18.
[61] Zhao X, Xu Q, Yang Y, Zhou G. Distributed distributionally robust optimization of distribution network incorporating novel battery charging and swapping station. Int J Electr Power Energy Syst 2024;155:109643.
[62] Qiu F, Ahmed S, Dey SS, Wolsey LA. Covering linear programming with violations. Inf J Comput 2014;26(3):531–46.
[63] Deng Y, Shen S. Decomposition algorithms for optimizing multi-server appointment scheduling with chance constraints. Math Program 2016;157(1):245–76.
[64] Jiang N, Xie W. The terminator: an integration of inner and outer approximations for solving Wasserstein distributionally robust chance constrained programs via variable fixing. Inf J Comput 2025;37(2):381–412.
[65] Zhang Y, Shen ZJM, Song S. Distributionally robust optimization of two-stage lot-sizing problems. Prod Oper Manag 2016;25(12):2116–31.
[66] Delage E, Ye Y. Distributionally robust optimization under moment uncertainty with application to data-driven problems. Oper Res 2010;58(3):595–612.
[67] Baron O, Milner J, Naseraldin H. Facility location: a robust optimization approach. Prod Oper Manag 2011;20(5):772–85.
[68] Chen W, Sim M, Sun J, Teo C-P. From CVaR to uncertainty set: implications in joint chance-constrained optimization. Oper Res 2010;58(2):470–85.
[69] Nemirovski A, Shapiro A. Convex approximations of chance constrained programs. SIAM J Optim 2007;17(4):969–96.
[70] Zymler S, Kuhn D, Rustem B. Distributionally robust joint chance constraints with second-order moment information. Math Program 2013;137(1):167–98.
[71] Chen W, Sim M. Goal-driven optimization. Oper Res 2009;57(2):342–57.
[72] Duran MA, Grossmann IE. An outer-approximation algorithm for a class of mixed-integer nonlinear programs. Math Program 1986;36(3):307–39.
[73] Bonami P, Biegler LT, Conn AR, Cornuéjols G, Grossmann IE, Laird CD, et al. An algorithmic framework for convex mixed integer nonlinear programs. Discrete Optim 2008;5(2):186–204.
[74] Fletcher R, Leyffer S. Solving mixed integer nonlinear programs by outer approximation. Math Program 1994;66(1):327–49.
[75] Lombardo T, Paoli L, Pales AF, Gul T. The battery industry has entered a new phase. Tech Rep: IEA; 2025.
[76] Fathollahi A, Gheisarnejad M, Boudjadar J, Homayounzadeh M, Khooban M-H. Optimal design of wireless charging electric buses-based machine learning: a case study of Nguyen-Dupuis network. IEEE Trans Veh Technol 2023;72(7):8449–58.
[77] Qu K, Xu X, Chen A. Dynamic route redundancy-oriented strategic planning towards resilient transportation networks. Transport Res C Emerg Technol 2026;184:105503.
[78] Xin X, Zhang T, Xiang Z, Liu M. Battery electric vehicle transportation network robust pricing-infrastructure location model with boundedly rational travelers. Appl Energy 2025;386:125606.